Transient response to changes in uplift rates in the northern Atlas-Meseta system (Morocco)

R. Clementucci, P. Ballato, L.L. Siame, C. Faccenna, S. Racano, G. Torreti, R. Lanari, L. Leanni, V. Guillou

Transient response to changes in uplift rates in the northern Atlas-Meseta system (Morocco)

Clementucci R.[1,2*], Ballato P.[1], Siame L. L.[2], Faccenna C.[1,3], Racano S.[4], Torreti G.[1], Lanari R.[5], Leanni L.[2], Guillou V.[2]

[1] *Dipartimento di Scienze, Università Roma Tre, Largo San Leonardo Murialdo 1, 00146 Rome, Italy*

[2] *Aix-Marseille Univ., CNRS, IRD, INRAE, Collège de France, CEREGE, Aix-en Provence, France*

[3] *GFZ-German Research Centre for Geosciences, Potsdam, Germany*

[4] *Institute for Geosciences, University of Potsdam, Potsdam, Germany*

[5] *Dipartimento di scienze, Università di Firenze, Italia*

**Corresponding author:* rclementucci@ethz.ch

Current address: Department of Earth Sciences, ETH Zurich, Zurich, Switzerland.

Keywords: landscape evolution, cosmogenic nuclides, transient topography, quantitative geomorphology, Atlas Mountains

Abstract

Transient topography represents an opportunity for extracting information on the combined effect of tectonics, mantle-driven processes, lithology and climate across different temporal and spatial scales. The geomorphic signature of transient conditions can be used to unravel landscape evolution, especially in areas devoid of stratigraphic constraints. The topography of the Western Moroccan Meseta domain (WMM) is characterized by elevated non-lithological knickpoints, that delimit an uplifted relict landscape, implying a transient response to a change in uplift rate that occurred during the Cenozoic. Here, we determine denudation rates of selected watersheds and bedrock outcrops from cosmogenic nuclides and perform stream profile, regional and basin-scale geomorphic analysis. Denudation rates of the relict and the rejuvenated landscape range from 15 to 20 m/Myr and from 30 to 40 m/Myr, respectively. Rock uplift rates from river-profile inversions are 10-25 m/Myr from 45 to 22 Ma and 30-55 m/Myr from 22 to 10 Ma. Despite the different time scales, the inverted rates are

consistent with ^{10}Be averaged denudation rates (15-20 and 30-40 m/Myr) and river incision values from Pleistocene lava flows (<10 and ~50 m/Myr) for the rejuvenated and relict regions of the WMM. These results agree with geological data and indicate that the observed ~400 m of surface uplift in the WMM started to develop possibly during the early Miocene (first phase). Given the wavelength of the topographic swell forming the topography of the WMM, uplift is here interpreted to reflect localized crustal thickening through magma addition or lithospheric thinning through mantle delamination. More recently, the occurrence of late Miocene marine sediments at ~1200 m of elevation indicates that the adjacent Folded Middle Atlas during the last 5-7 Ma experienced surface uplift at ~170-220 m/Myr. Considering the cumulative amount of surface uplift that varies eastward from 400 to 800 and 1200 m from the Meseta to the Tabular and the Folded Middle Atlas, as well as the spatio-temporal pattern of alkaline volcanism (middle Miocene and Pliocene to Present), we suggest that the most recent episode (second phase) of surface uplift was induced by a larger-scale process that most likely included upwelling of asthenospheric mantle and to a lesser extent crustal shortening in the Folded Middle Atlas.

1. Introduction

The competition between crustal deformation, mantle driven uplift and surface processes modulates the growth and the decay of topography across diverse temporal and spatial scales (England and Molnar, 1990; Faccenna and Becker, 2020; Babault et al., 2022). Analytical solutions and numerical models suggest that topography should attain a steady state configuration when uplift is balanced by surface erosion (Whipple, 2001; Willet and Brandon, 2002). Conversely, when such a balance is not respected the landscape should be in disequilibrium conditions (*i.e.*, a transient landscape; *e.g.*, Olivetti et al., 2016; Godard et al., 2019; Clementucci et al., 2022; 2023). Transient landscapes represent the unique possibility to unravel the topographic evolution in areas devoid of stratigraphic constraints since the landscape still contains geomorphological features relative to the pre-

perturbation stage. The transience results from different causes, such as base-level falls, drainage reorganizations, climate changes and/or variations in uplift rates at crustal and deeper scales (*e.g.*, Snyder et al., 2002; Roberts and White, 2010; Miller et al., 2013, Ballato et al., 2015; Sembroni et al., 2017; Gallen, 2018; Fernandes et al., 2019; Faccenna and Becker, 2020; Racano et al., 2021; Lanari et al., 2022). Therefore, the topography represents the superimposition of processes operating at multiple timescales and acting at different rates, wavelengths, and amplitudes. Although diverse approaches have been used to unpick these different signals, the combination of quantitative geomorphology with denudation data from cosmogenic nuclides and river profile inversion represents a powerful tool to infer the magnitude, timing, and rates of uplift through time (Miller et al., 2013; Goren et al., 2014; Pastor et al., 2015). This comprehensive approach allows for exploration of the uplift history of areas lacking stratigraphic constraints, with the potential to deconvolve the signals of topographic growth operating at different spatial scales. The surface expression of large-scale uplift and associated causes, in fact, remains often elusive mostly because the rates at which uplift occurs is poorly understood. Accordingly, the integrated approach outlined above can provide fundamental insights into geodynamic processes.

In this study, we focus on the Western Moroccan Meseta and the adjacent Tabular Middle Atlas, two tectonically quiescent domains of the Atlas-Meseta system (Fig. 1b). Despite quiescence, these relief features are characterized by elevated, extensive, low-gradient erosional surfaces bounded by steep hillslopes that are adjusting through fluvial incision, to a relative base level drop. This landscape is considered to represent a transient topography resulting from a Neogene phase of large-scale surface uplift, most likely driven by mantle upwelling (*i.e.*, topographic rejuvenation, *e.g.*, Missenard et al., 2006; Babault et al., 2008; Frizon de Lamotte et al., 2009; Miller and Becker, 2014; Clementucci et al., 2023). The relict surfaces are characterized by a protracted phase of hillslope lowering, documented by low temperature thermochronology. Data suggests slow hillslope exhumation rates since the latest Cenozoic (< 28 m/Ma if we consider a maximum cooling of 50°C over the last 70 Ma and a geothermal gradient of 25 °C; see thermal modelling in Barbero et al., 2010 and also the recent

79 review of Charton et al., 2020). These conditions provide a natural setting for investigating the
80 mechanisms of large-scale uplift in tectonically inactive (or slow deforming) areas and quantifying
81 rock uplift changes through time since the relict topography retains features of the pre-uplift event.

82 In this work, we combined denudation rates derived from in situ-produced cosmogenic nuclides
83 (^{10}Be) with regional and basin-scale geomorphic analysis and river profile inversions. Specifically,
84 we determined bedrock outcrops and basin-wide denudation rates from river-borne sediments to
85 gauge them with basin-averaged geomorphic metrics (slope, local relief, and normalized steepness
86 index). In addition, we estimated the magnitude of base-level fall by projecting the upper relict
87 channels toward the present-day river mouth (*e.g.*, Miller et al., 2013; Sembroni et al., 2020). This
88 allowed us to quantify the long-term magnitude of uplift of the Western Moroccan Meseta and the
89 surrounding Tabular and Folded Middle Atlas domains. Moreover, we reconstructed the Cenozoic
90 uplift history of the entire northern Atlas-Meseta system by combining the rock uplift evolution
91 through time inferred from fluvial modelling with available geological data. Our results show
92 consistent rates of denudation and rock uplift of the rejuvenated and the relict portions of the
93 landscape through time and highlight the transient adjustment of hillslope and channels in response
94 to a Cenozoic increase in rock uplift rates. Finally, we retraced back in time the uplift and the
95 topographic evolution of the northern sector of the Atlas-Meseta orographic system and discussed
96 possible driving mechanisms of the topographic rejuvenation.
97

98 ## 2. Geological setting

99 The Atlas-Meseta of Morocco (NW Africa) includes mountain ranges (Anti-Atlas, High Atlas and
100 Middle Atlas) elevated tabular areas (Western Meseta, Tabular Middle Atlas and High Plateaus), and
101 sedimentary basins (Missour and Saiss among others; Fig. 1a). The WSW-ENE oriented, 4-km-high
102 High Atlas represents the highest mountain range of the Atlas-Meseta system. It consists mainly of
103 Mesozoic-Cenozoic syn- to post-rift deposits that were uplifted in the Eocene and Miocene (Arboleya

et al., 2004; Lanari et al., 2020a). The central sectors of the High Atlas merge towards the NE with the SW-NE-striking Middle Atlas (Fig. 1a). This range is formed by the same deposits of the High Atlas that were deformed most likely from the late Miocene, but with some angular unconformities suggesting a more complex Meso-Cenozoic history of deformation and sedimentation (Charrière, 1984). Topographically, the Middle Atlas can be divided into two morpho-structural domains known as the Tabular and Folded Middle Atlas (TMA and FMA; Fig. 1b), which are commonly interpreted as the flank (footwall) and the depocenter (hanging wall) of a Mesozoic rift, respectively (Gomez et al., 1996; 1998). The TMA domain ranges between 1500 and 2000 m of elevation and consists of Mesozoic limestones that are slightly tilted westward. The FMA reaches 3000 m of elevation and includes north-west- to south-east-verging folds mostly detached from the underlying basement along Triassic evaporites (Charrière, 1984; Gomez et al., 1998). The folded range is bounded to the northwest by the North Middle Atlas fault (NMAF) and to the southeast by the South Middle Atlas Fault (SMAF; Fig. 1b). The elevated Western Moroccan Meseta (WMM) and High Plateau (HP) rises to an elevation of 1500 m, without any evidence of Cenozoic tectonic deformation (Gomez et al., 1999; Barbero et al., 2010). Particularly, the WMM is characterized by a complex assemblage of Paleozoic rocks deformed during the Variscan orogeny (Hoepffner et al., 2005; Fig. 1b). This includes Ordovician, Silurian, and Devonian schists and metasedimentary rocks, locally intruded by late Carboniferous granitoids (320 and 270 Ma; Hoepffner et al., 2005 and references therein). This domain is partially covered by undeformed Mesozoic and Eocene marine sedimentary rocks (*e.g.*, Phosphatic series; Salvan, 1954; El Kiram et al., 2019; El Attmani et al., 2021). The Rif Mountains to the north reaches peaks of up to 2500 m and represents a fold and thrust belt that experienced NW-SE shortening due to the convergence of Africa and Eurasia (Jolivet and Faccenna, 2000; Abbassi et al., 2020; Agharroud et al., 2021). There, contractional deformation migrated southward until 8 Ma when the outermost tectonic units where emplaced onto the South Rifian Corridor (Krijgsman et al., 1999; Capella et al., 2018; Abbassi et al., 2020; 2022).

The High and Middle Atlas domains are characterized by strain partitioning with a total amount of shortening of ~24%, accommodated by both thrust and oblique/strike-slip faults (Gomez et al., 1999; Lanari et al., 2020b). The amount of shortening across the thrust faults ranges between ~12% and 15 % (Missenard et al., 2006; Domenech et al., 2018; Lanari et al, 2020a; 2023) suggesting that crustal thickening is insufficient to isostatically support the modern topography (Arboleya et al., 2004; Missenard et al., 2006). Moreover, geophysical studies highlight the presence of an anomalously thin lithosphere beneath the entire Atlas-Meseta system (Miller and Becker, 2014; Miller et al., 2015). This is associated with continental intraplate volcanism that seems to be coeval with the main tectonic events (Missenard et al., 2006; El Azzouzi et al., 2010; Lanari et al., 2020a). The lavas are well exposed in the FMA, TMA, the WMM over a surface of about 960 km^2 and have a geochemical affinity with the Canary mantle plume composition ranging from basanite to alkali basalt (Duggen et al., 2009; El Azzouzi et al., 2010). The late Cenozoic phase of uplift is documented by the occurrence of late Miocene (Messinian) shallow-water marine deposits in the Skoura basin at ~1200 m of elevation (Babault et al., 2008) and the progressive shallowing upward trend of the Miocene marine sediments of the Saïss and Guercif basin (Fig. 1a; Krijgsman et al., 1999).

3. Methods

3.1. Topographic, stream analysis and long-term incision

A Shuttle Radar Topography Mission Digital Elevation Model (SRTM DEM, pixel size of 30 m) was used to extract the drainage network. Hillslope metrics, such as slope and local relief with a circular sampling window of 2.5 km radius, as well as channel and basin metrics were extracted using ArcGIS and the MATLAB software packages TopoToolbox (Schwanghart and Scherler, 2014) and Topographic Analysis Kit (TAK, Forte and Whipple, 2019), together with additional MATLAB functions (*e.g.*, Gallen, 2017). The relationships between river channel steepness and erosion/uplift rates have been demonstrated in various geological settings (Kirby and Whipple, 2012). In

detachment-limited conditions, these relationships are modulated by the stream-power model, which can be integrated, assuming spatially invariant uplift and erodibility, to estimate the integral quantity χ (details in the section S1; Perron and Royden, 2013). This allows transforming river longitudinal profiles to χ versus elevation (z) plots (here and thereafter defined as χ - z plot). Consequently, the slope in χ space is defined as the steepness index (k_s) when the reference area (A_0) is equal to 1. To compare k_s values of longitudinal profiles, a reference concavity index (θ_{ref}) of 0.45 is applied to derive the normalized channel steepness indices (k_{sn}; Kirby and Whipple, 2012 and references therein). The θ_{ref} was calculated by minimising the scatter in χ space of all rivers draining the study area (Perron and Royden, 2013; Goren et al., 2014; Fig. S1). Our θ_{ref} coincides with the value typically used to derive normalised channel steepness (Snyder et al., 2000; Kirby and Whipple, 2012).

Knickpoints were identified and discretized based on the shape of the streams in the longitudinal profiles and the χ -z plots and using available geological maps (Service Géologique du Maroc) and satellite imagery (Google Earth). Importantly, non-lithological knickpoints cluster around similar χ values and separate stream segments with different k_{sn} values (Perron and Royden, 2013; Clementucci, 2022). Using this approach, the knickpoints were divided into non-lithological, minor, lithological and man-made dam. Streams with knickpoints identified as transient (non-lithological) were used for reconstructing river projections to estimate the magnitude of long-term incision. Such profiles can be reconstructed using the k_{sn} values (θ_{ref} = 0.45) of the river segments upstream of the non-lithological knickpoints in the χ space, assuming that the paleo-river network remained approximately the same through time (Perron and Royden, 2013; Smith et al., 2022). Full details of equations and stream analysis are provided in the Supplementary material.

3.2. ^{10}Be-derived denudation rates

177 We measured the concentration of in situ-produced cosmogenic ^{10}Be in quartz from seven river-borne
178 samples collected in active channels and from four bedrock outcrops (Fig. 1c; Table 1). The only
179 lithologies exposed in the WMM that contain quartz are Paleozoic basement rocks such as schists,
180 metasedimentary rocks, and granites. Our sampled catchments cover most of this area (Figs 1b and
181 S2), from the elevated relict to the steeper landscape portions. In one case we sampled a catchment
182 with Paleozoic rocks at the periphery of the uplifted area (sample 53) to compare denudations rates
183 from different sectors of the WMM (Fig 1c). The basin-wide denudation rates were determined only
184 from quartz-bearing rocks, which usually represent 50 to 100% of the total area of the sampled
185 catchments (Table S1). The portions of the sampled catchments with Mesozoic limestones were not
186 considered in the scaling modelling (Clementucci et al., 2022 and references therein). Details of
187 sample preparation, from the initial mineral separation to the final conversion of in situ-produced
188 ^{10}Be to basin-wide denudation rates are provided in the Supplementary material S2. Catchments 58,
189 59, 60 and 62 are sub-catchments of two larger basins named 61 and 63, while catchment 53
190 corresponds to the westernmost sampling location (Fig. 1c). The upstream areas range between 30
191 and 100 km^2 and 320 and 350 km^2 for the sub-catchments and the larger basins, respectively. In
192 particular, we selected samples 58 and 59 upstream of the low-relief surfaces and samples 61 and 63
193 downstream of the relict landscape to extract the denudation rates of the adjusted and steeper
194 topography. Catchments 53, 58, 59, 62 and 63 are characterized by uniform quartz-bearing
195 lithologies. Conversely, the contribution of quartz, in catchments 60 and 61, is mostly from two
196 granite massifs exposed in the highest topography of the Moroccan Meseta region. To quantify the
197 local denudation rates of the granite massifs forming the landscape of the western Meseta, we sampled
198 four bedrock outcrops: two from the summit of an erosional surface (samples 56A, 56B) and two
199 from sub-horizontal ridge crests located close to the margin of the relict topography (samples 57A,
200 57B, Table 1 and Fig. 1c).

201 In situ-produced ^{10}Be concentrations were converted to basin-wide denudation rates and bedrock
202 erosion rates using the MATLAB scripts of Balco et al. (2008), which are based on the time-

dependent scaling functions of Stone (2000)'s scheme that consider three different categories of particles responsible for the in-situ production of ^{10}Be (Braucher et al., 2011). The geomorphic shielding (Dunne et al., 1999), scaling factor of Stone (2000) and the mean elevation of sampled catchments were determined for each pixel of the digital elevation model (DEM), considering only the areas contributing with quartz-bearing lithologies. In the scaling model, λ describes the radioactive decay constant of ^{10}Be. Denudation rates from ^{10}Be concentrations were calculated using a ^{10}Be sea level high latitude production rate of 4.02 ± 0.33 atoms ^{10}Be (g-SiO_2)/yr (Borchers et al., 2016), and half-lives of (1.387 ± 0.012) × 10^6 years (Chmeleff et al., 2010; Korschinek et al., 2010). At cosmogenic steady-state, the cosmogenic ^{10}Be in river-borne quartz mineral records a time integrated spatially averaged denudation rate, which represents fluvially mixed denudation products of all the processes occurring in each watershed (Granger et al., 1996). This integration occurs over the time needed to remove one attenuation length (*e.g.,* roughly 60 cm; Lal, 1991).

We also applied a sediment mixing correction to estimate a value of denudation for the downstream knickpoint portion of the catchment 63 (basin 64), knowing the denudation and drainage area of the whole catchment and the upper sub-catchment, upstream of the non-lithological knickpoints (Fig. 2; according to Granger et al., 1996; Miller et al., 2013; Rosenkranz et al., 2018):

$$D_{1-2} = \frac{D_1 A_1 - D_2 A_2}{A_1 - A_2} \quad (1)$$

where $A_1 - D_1$ and $A_2 - D_2$ are the drainage area and basin-wide denudation rate of the whole catchment and above the non-lithological knickpoint, respectively. $D_{1\text{-}2}$ is the basin-wide denudation of the adjusted topography downstream of non-lithological knickpoints.

3.3.Predicted ^{10}Be-derived denudations and incision of volcanic bedrock

The basin-averaged k_{sn} values, precipitation rates (IMERG data; Huffman et al., 2015), slope and local relief for the portions of the sampled catchments that include only quartz-bearing lithologies were extracted for comparing ^{10}Be-derived denudation rates. The comparison between denudation rates and k_{sn} allowed extracting the averaged erodibility parameter K for basement rocks in the Western Meseta and constraining n equal to 1. We also evaluate the power best-fit to better explore the relationship between channel steepness and erosion, and evaluate the power-law coefficients, K and n. Finally, values of k_{sn} values were directly converted to denudation rates (see details in Adams et al., 2020, and Clementucci et al., 2022).

To compare our inferred and measured, short-term denudation rates, with longer-term rates we estimated fluvial incision rates by using the 1-Myr-old lava flows as a temporal and geometrical benchmark because they were emplaced over the relict and the rejuvenated landscape of the WMM domain (Tephrite and Basanite data from Rachidi, 1995).

3.4.Rock uplift history

To unravel the rock uplift rates over time, we performed a linear inversion of the rivers draining the Paleozoic basement in the Moroccan Meseta domain. We constrained the averaged erodibility value (K) of the Paleozoic basement rocks, using the stream power river incision model ($K = E/k_{sn}^{n}$) for n = 1. The K was estimated using the forced-origin linear regression in the plot k_{sn} and denudation rates. Although the variation of K over time is difficult to constrain, our averaged estimate can be considered reliable because short-term denudation rates are consistent with the long-term exhumation rates derived from thermochronological data over other quiescent sectors of the Atlas-Meseta system (*e.g.*, Anti-Atlas and Haouz basin; Lanari et al, 2020a; Clementucci et al., 2022; Western Meseta; Barbero et al., 2010). Assuming block uplift conditions in a selected catchment (no spatial uplift variations) and n = 1, the travel time of a perturbation along a river profile (τ) is given by:

$$\tau = \int_{xb}^{x} \frac{dx'}{K A_0^m A(x')^m} \quad (2)$$

By removing K from Equation (1) we obtain χ. Following the approach of Goren et al. (2014), a non-dimensional uplift can be inferred from the integration of the stream-power model by assuming that trunks with same χ share a common uplift history and organizing the equation in a matrix form for each data point:

$$\boldsymbol{A^* U^* = z} \quad (3)$$

where $\boldsymbol{A^*}$ is an $N \times q$ matrix, q is the number of χ intervals, $\boldsymbol{U^*}$ is the non-dimensional uplift and $\boldsymbol{z}$ is elevation. This is an overdetermined inverse problem, as there are more known data points than unknown parameters. As such, a least-squares estimate for U^* is used (Goren et al., 2014):

$$\boldsymbol{U^* = U^*_{pri} + (A^{*T} A^* + \Gamma^2 I)^{-1} \circ A^{*T} (z - A^* U^*_{pri})} \quad (4)$$

Where Γ is a dampening coefficient that determines the smoothness imposed on the solution, $\boldsymbol{I}$ is the $q \times q$ identity matrix and U^*_{pri} represents the prior guess for U^*, estimted by taking the average slope of the χ-plot (Goren et a., 2014) . In this way, from the integration of the stream-power model, χ and U^* can be scaled for K to infer rock uplift rates (U) and time (τ):

$$U = K A_0^m U^* \quad (5)$$

$$\tau = \frac{\chi}{K A_0^m} \quad (6)$$

To reduce the noise, we removed streams with a length lower than 10 km. The linear inversion approach is built on the assumption of spatially uniform uplift, which to a first approximation, can be considered reasonable given that the analysed catchments do not cross any fault that may have been active during the late Cenozoic. Moreover, the analysed catchments are entirely in the WWM where they occupy relatively narrow areas, and hence do not record major along-strike variations in uplift rates. Thus, adopting this approach, by combining the inversions from different catchments, it is also possible to investigate spatial variations in rock-uplift histories (Pavano et al., 2021; Racano et al, 2021; Zhong et al., 2022).

4. Results

4.1. Topographic and river analysis

The WMM domain consists of a NE-SW striking, ~ 130 x 260 km topographic swell, with a maximum elevation of ~1500 m, and a low relief topography that locally has been deeply dissected by fluvial incision (Figs. 3 and 4). Within the WMM, a series of smaller scale geomorphic features such as summit erosional surfaces, ridge crests and fluvial terraces developed onto and inset into the lava deposits are visible (Figs. 4 and 5). The TMA presents a tabular, low-relief topography while the FMA is characterized by an alternation of steep ridges and wide, low-slope valleys (Figs. 3 and S3). Based on the geometry of the river network, the study area was divided into the Central-Western Meseta (CWM), the North-Western Meseta (NWM), and the South-Western Meseta (SWM). The CWM is characterized by rivers draining directly into the Atlantic Ocean, while the rivers of the NWM and SWM represent the main respective tributaries of the Atlantic draining Oued Sebou and Oum Er Rbia, (Fig. 3a). A set of regionally widespread non-lithological knickpoints occur at different elevations in the three domains. These features mark a sharp variation in the k_{sn}, local relief and slope between the deep valleys and the upstream landscape (dashed line in Figs. 3a, 3b and S3). Particularly, high values of k_{sn} (> 80 $m^{0.9}$; Fig. 3b), slope (> 25°; Fig. S3a), and local relief (> 500 m; Fig. S3b), are found in the FMA domain and in the downstream portions of the non-lithological knickpoints of the WMM and the TMA domains. The lowest values of topographic and channel parameters are observed in the lower portions of the landscape (Oum Er Rbia and Sebou basins) and upstream of the non-lithological knickpoints (Figs. 3 and S3).

The NWM sector is characterized by transient longitudinal profiles. Most of the rivers flowing from the TMA and the WMM present lithological knickpoints between 1500 and 2000 m of elevation at χ values of 20 to 25 (Fig. 6a and 6b). A pattern of widespread non-lithological knickpoints is located

between 700 and 1500 m and is associated with a gradual increase in elevation from 200 to 450 km of distance from the river mouth (Fig. 6a and Table S2). These non-lithological knickpoints cluster at χ values of 13 – 17 and separate steep downstream segments from low-gradient upstream channels. A cluster of minor knickpoints is located at lower elevations and separates gentle downstream river segments from steeper upstream portions (Figs. 6a and 6b).

Rivers of the CWM sector show concave-up longitudinal profiles downstream of the non-lithological knickpoints and straight low-gradient upper segments (Fig. 6c). These non-lithological knickpoints present a progressive increase in elevation from 300 m close to the river mouth to ~1000 m upstream toward theTMA domain. Most of these non-lithological knickpoints cluster at χ values of 10 – 15, and separate downstream steep segments from low-gradient upstream portions (Fig. 6d). Downstream of these non-lithological knickpoints, the river segments are characterized by gentle low-gradient river profiles, which contain several minor knickpoints (Fig. 6c).

The SWM sector is characterized by both equilibrated and transient longitudinal profiles. The main slope break is located at high elevation, where two non-lithological knickpoints lie in the FMA domain (~1900 m and ~1500 m; Fig. 6e and 6f). The average elevations of the non-lithological knickpoints are 627 (σ= 116) m, 1255 (σ = 86) m and 1724 (σ = 135) m for the WMM, TMA and FMA domains, respectively (Table S2).

4.2. Long-term river incision

The magnitude of long-term river incision can be estimated by the difference between the reconstructed river profiles projected from the non-lithological knickpoints and the modern base level. Rivers draining the WMM domain (mainly from CWM and NWM sectors) show a mean long-term incision of 415 (2σ = 55) m, based on 33 river projections (Fig. 7a and Table S3). The mean values of long-term incision of rivers draining the TMA domain is 823 (2σ = 66) m, based on 8 river projections (Fig. 7a and Table S3). The river projections from the FMA domain show an average long-term incision of 1086 (2σ = 64) m, although based only on 2 rivers (Fig. 7a and Table S3).

There, rivers flow along the SWM sector. Overall, both elevations of the non-lithological knickpoints and magnitude of long-term incision increase progressively from the WMM to the TMA and FMA domains (Fig. 7b).

A few valleys of the WWM have been filled by Quaternary lava flows downstream and upstream of major non-lithological knickpoints (Fig. 1a). Subsequently, these lava flows were dissected through fluvial incision leaving well developed terraces. Downstream of major non-lithological knickpoints, the current valley floor is ~50 and ~100 m below the base and the top of the lava flows, respectively (Figs. 4 and 5b). Considering that the lava yielded radiometric ages of 1 ± 0.1 Ma (Rachdi, 1995), fluvial incision rates vary from ~100 ± 10 to ~50 ± 5 m/Myr, respectively. Importantly, the latter estimate (~50 ± 5 m/Myr) represents the amount of river channel lowering after the lava emplacement using the unconformity as a reference surface (strath of the terrace). Conversely, in the relict surfaces of the WMM domain the lava flows are poorly incised and the fluvial incision rate are <10 m/Myr (Fig. 4).

4.3. ^{10}Be-derived denudation rates

^{10}Be concentrations from the largest catchments of the WMM yield denudation rates of 19.8 ± 1.4 and 32.2 ± 2.3 m/Myr (samples 61 and 63; Fig. 1c and Table 1). Denudation rates from the sub-catchments located upstream of the relict landscape are 17.1 ± 1.3 and 19.5 ± 1.4 m/Myr (samples 58 and 59), whereas the sub-catchments downstream of non-lithological knickpoints present rates of 17.4 ± 1.2 and 40.0 ± 5.6 m/Myr (samples 60 and 62; Fig. 1c and Table 1). In the western side of the Moroccan Meseta, sample 53 yields a denudation rate of 14.8 ± 1.0 m/Myr. The unmixed rate from catchment 64 (*i.e.,* the denudation rate of the incised portion of the landscape of catchment 63, which was obtained by subtracting the contribution of the relict landscape of sub-catchment 59 and the area of the steep sub-catchment 62 downstream of non-lithological knickpoints; Fig. 2), yields a denudation rate of 35.2 ± 2.6 m/Myr. This shows a good match with the estimates of denudation from

the same sub-catchment 62 (Fig. 2 and Table S1). The sampled catchments are characterized by a uniform distribution of quartz, which is mostly sourced from the lower Paleozoic metamorphic basement, except for samples 60 and 61. These two basins are influenced by the occurrence of two large granite outcrops located in the high-standing low relief surface of the WMM (Fig. 4), which most likely provided more quartz than the Paleozoic metamorphic rocks. Local denudation rates of bare bedrock surfaces on the summit plateau (relict surface) and on the ridge crests of the granite massif vary from 3.5 ± 0.2 to 4.1 ± 0.3 m/Myr (samples 56A, 56B), and from 13.1 ± 0.9 to 14.4 ± 1.0 m/Myr (samples 57A, 57B), respectively (Table 1). It is worth noting that the denudation rates of the granitic ridge crests: 1) are significantly higher than the rates of the flat summit surfaces, and 2) are close to the values determined for the watersheds of samples 60 and 61, where the two granite massifs are exposed and may provide most of the quartz that yielded the measured ^{10}Be concentration.

4.4. Basin-wide denudation rates versus topographic metrics

The basin-averaged k_{sn} values range from 16.7 to 53.5 $m^{0.9}$ (Fig. 8a and Table S1), while basin-averaged slope values vary from 6 to 13° (Fig. 8b and Table S1) and the basin-averaged local relief range from 222 to 440 m (Fig. 8c and Table S1). The topographic and channel metrics exhibit a medium to low correlation with the basin-wide denudation rates with R^2 of 0.13, 0.61 and 0.71 for k_{sn}, slope and local relief, respectively (dashed lines in Fig. 8a, 8b, 8c). However, a stronger correlation between the topographic metrics and basin-wide denudation rates is obtained considering only the catchments characterized by a homogeneous distribution of bearing-quartz lithologies of the Paleozoic basement (*i.e.*, excluding samples 60 and 61, which quartz is mostly sourced from the granites above the elevated flat surfaces). In this case, the coefficient of correlation increases to 0.76, 0.87 and 0.97 for the basin-averaged k_{sn} values, slope, and local relief, respectively (Fig. 8a, 8b, 8c). The lowest topographic and channel metrics are observed for samples 53, 58 and 59, which represent the westernmost sample (53) and the samples upstream of the non-lithological knickpoints.

Conversely, samples 62 and 64 (downstream of the non-lithological knickpoints) show the highest values of basin-averaged k_{sn} values, slope and local relief, whereas samples 60, 61 and 63, show slightly lower values, because they represent the mixed estimates, giving that both the upstream and downstream portions of the catchments are contributing (Fig. 8a, 8b, 8c and Table S1). Finally, basin-wide denudation rates are poorly correlated with the basin-averaged precipitation (R^2=0.38; Fig. 8d).

4.5. Timing: base-level fall history

To constrain the base level history, the linear inversion of six river profiles has been performed using n = 1, m/n = 0.45 and K of 7.34 ± 0.58 x 10^{-7} $m^{0.1}$/yr. The parameter n = 1 describes the linear relationship between the erosion rates and k_{sn} (Fig. 8a), as expected for inactive to slow tectonic settings (Godard et al., 2019; Clementucci et al., 2022). The estimation of n has been made testing the stream-power law fits, confirming that the assumption of n = 1 is reasonable (Fig. 8a). The six catchments were selected as they flow over the same rocks from which the K value was estimated (Figs. 9a and S5, S6). Results show similar rock uplift histories (Figs. S5 and S6), which are summarized in Figure 9b with the mean and the standard error and deviation of the six inversions. Overall, we observe almost constant rock uplift rates of 15-20 m/Myr from 30-33 until ~25 Ma, followed by an increase up to ~40 m/Myr between 20 and 15 Ma and by a general decrease to ~25 m/Myr during the last 10 Ma (Fig. 9b). Importantly, within this decreasing trend, a peak in rock-uplift occurs around 5-6 Ma with values of up to 35 m/Myr despite the large standard deviation.

5. Discussion

5.1.Transient topography in Western Moroccan Meseta and Middle Atlas

The study area is characterized by high-standing relict surfaces bounded by non-lithological knickpoints and deeply incised valleys downstream of these knickpoints. This elevated landscape is characterized by low k_{sn} and include low-topographic slopes and local relief surfaces carved onto Paleozoic metamorphic rocks and Mesozoic limestones that gently dip toward the western sectors (Figs. 3, 4, 5; Barbero et al., 2010; Barcos et al., 2014). A few lithological knickpoints lie at about 1500 m of elevation at the boundary between the WMM and TMA domains (see bold yellow points in Fig. 6a, 6b). These knickpoints are marked by a local variation in k_{sn} values and other topographic metrics (slope and local relief) and coincide with a ~500-m-high morphological escarpment representing the stratigraphic contact between the Paleozoic basement and the undeformed Jurassic limestones, reflecting a sharp change in rock erodibility. Conversely, downstream of non-lithological knickpoints the landscape is characterized by steep slopes and k_{sn} values at regional scale (Figs. 3, 4, 5 and S2). This topographic dichotomy suggests that the landscape and hence the river network is not in equilibrium (Crosby and Whipple, 2006; Kirby and Whipple, 2012).

The disequilibrium condition can be explained through several processes, such as drainage reorganization, climate change, eustatic sea-level fall and tectonic uplift (Snyder et al., 2002; Crosby and Whipple, 2006; Kirby and Whipple, 2012; Miller et al., 2013; Boulton et al., 2014; Ballato et al., 2015; Rixhon et al., 2017; Stokes et al., 2017). In the WMM, a base-level fall due to eustatic forcing is unlikely to be the source of the observed non-lithological knickpoints, because it cannot explain the pattern of k_{sn} values of the river network. Specifically, a wave of knickpoints due to eustatic causes cannot exhibit any major slope break in the chi-space because it is not associated with variations in uplift rate or rock erodibility (Wobus et al., 2006; Kirby and Whipple, 2012; Perron and Royden, 2013). Moreover, there is no geological data documenting a major and protracted sea level drop during the late Cenozoic (Miller et al., 2020) and the glacial-interglacial cycles occurred over the last 1 Ma would result in multiple phases of incision and filling of the coastal area (*e.g.*, Marra et al., 2016), rather than a wave of incision reaching the upper reaches of the Meseta. Drainage reorganization could explain the increase in long-term fluvial incision downstream of the knickpoints

due to a gain in drainage area and hence in water discharge (*e.g.*, Yang et al., 2015). However, the non-lithological knickpoints are observed in the watersheds of all domains (WMM, TMA and FMA; Fig. 3), even in small catchments where there is no evidence of drainage reorganization (*e.g.*, wind gaps, knickpoints due to capture processes among others), as instead observed in the Moulouya basin to the east of FMA (Bartz et al., 2018). Furthermore, increased erosion due to enhanced of average precipitation can also be discarded because it should produce a decrease in the channel slopes downstream of non-lithological knickpoints (Miller et al., 2013; Marder and Gallen, 2023; Figs. 3 and S2). Importantly, the non-lithological knickpoints are characterized by a major upstream decrease in k_{sn} values even across the same lithology as documented in the χ space plots (Fig. 6) and by changes in the topographic slope and local relief at the regional scale (Figs. 3 and S2). This indicates that the knickpoints separate portions of the landscape eroding at different rates (*e.g.*, Crosby and Whipple, 2006; Kirby and Whipple, 2012; Boulton et al., 2014; Olivetti et al., 2016). Consequently, the portion with steep channels downstream of the knickpoints records the response of the fluvial system to an increase in rock uplift rates, while the upstream low relief topography (relict landscape; Fig. 4) records the pre-uplift conditions, as also observed in the others domains of the Atlas-Meseta system (*e.g.*, High Atlas, Siroua and Anti-Atlas range; Boulton et al., 2014; Zondervan et al., 2020; Clementucci et al., 2023). Overall, these observations indicate that the study area experienced a recent topographic rejuvenation (regional, large-scale surface uplift) as documented in other regions worldwide exhibiting similar topographic patterns (Calvet et al., 2015; Miller et al., 2013).

Conversely, minor knickpoints lying at lower elevations can be attributed to Quaternary climate change or a second increase in uplift rates (Hancock and Kirwan, 2007; Molnar and England, 1990). A similar pattern of minor knickpoints has been described also for the Anti-Atlas domain, where their origin is still enigmatic (Clementucci et al., 2023). In the Western Meseta, these less elevated knickpoints do not present a pronounced break point along the river profiles, but they are evenly distributed along the rivers. Moreover, an increase in rock-uplift is shown around 5-6 Ma in the river-

449 profile inversions. These observations suggest a possible upward knickpoint migration following a
450 second topographic rejuvenation event (*i.e.*, a second increase in uplift rates at 5-6 Ma), which most
451 likely occurred at a larger wavelength from the WMM to the TMA and the FMA (and possibly the
452 HP), as testified by uplifted Messinian marine sediments of the Skoura and Saiss basins (Babault et
453 al., 2008).

454

455 **5.2. Erosional dynamics in the rejuvenated Western Moroccan Meseta**

456 The characterization of a transient landscape is critical for understanding the dynamics of a landscape
457 that includes the coexistence of portions that are in equilibrium with past and present uplift rates. In
458 the Western Meseta the lowest bedrock denudation rates are from granite exposed on the tops of the
459 summit surfaces (3.5 ± 0.2 and 4.1 ± 0.3 m/Myr) while the highest rates are from a similar granite
460 exposed along small ridge crests (13.1 ± 0.9 to 14.4 ± 1.0 m/Myr in Table 1). This four-fold difference
461 is presumably caused by different hillslope processes and higher physical and chemical weathering
462 assuming the same exposure time (Riebe et al., 2004). This demonstrates the key role of hillslope
463 topographic gradients and weathering processes in controlling denudation rates from bedrocks (*e.g.*,
464 Meyer et al., 2010; Godard et al., 2019). In our case, the highest denudation rates occur on the ridge
465 morphologies, at the margin of relict landscape, suggesting an abrupt increase in denudation and
466 hillslope erosion at the transition between the rejuvenated and relict topography, indicating a strong
467 control of the geomorphic domain on the ^{10}Be-derived denudation (Figs. 4 and 5).

468 Interestingly, the rates of denudation from the ridge crests (samples 57A and 57B) are very similar to
469 those from the watersheds of the same areas (samples 60 and 61). This may be due to the widespread
470 exposure within the catchments of the relict surface sculptured onto the granite rocks that contains a
471 higher amount of quartz than the adjacent metamorphic rocks. These quartz-rich granite rocks erode
472 at relatively low rates (~4 m/Myr) with respect to the basin-wide denudation rates from the

473 catchments composed of metamorphic rocks (> ~17 m/Myr) and hence have a higher ^{10}Be
474 concentration than the metamorphic basement. The greater amount of quartz sourced from the relict
475 landscape appears to increase the final ^{10}Be concentration for catchments 60 and 61, producing a
476 decrease in denudation rate estimates. This process is further corroborated by the poor sensitivity of
477 these two watersheds to the linearity between basin-wide denudation rates and topographic metrics
478 that are systematically lower than expected (Fig. 8). Low denudation rates are also observed in
479 watersheds 58 and 59, located upstream of non-lithological knickpoints within the relict portion of
480 the WMM landscape where values of basin-averaged k_{sn}, slope and relief are low. These low
481 denudation rates are consistent with those inferred from the thermochonological data (Barbero et al.,
482 2010) averaged over the last 70 Ma and reflect the erosional decay of topography during a long period
483 of relative base level stability (Calvet et al., 2015). Conversely, watersheds 62 and 63 present higher
484 denudation rates because they receive most of the quartz from the incised landscape downstream of
485 non-lithological knickpoints since the distribution of quartz-bearing rocks is uniform. In this case
486 higher rates reflect the increase in uplift rates as documented in other regions that experienced a
487 topographic rejuvenation (e.g., Olivetti et al., 2016; Miller et al., 2013; Clementucci et al., 2022).

488 In slow tectonic settings, there is usually a poor correlation between basin-averaged k_{sn} values and
489 denudation rates, and this is generally attributed either to the lithological control on the landscape
490 dynamics or to a decoupling between hillslope and channel incision (*e.g.*, Olivetti et al., 2016; Peifer
491 et al., 2021; Clementucci et al., 2022). Our data show a good correlation between denudation rates
492 and topographic metrics, despite the high degree of transience in the landscape, suggesting that the
493 landscape is not affected by any lithological control and/or decoupling process, except for catchments
494 60 and 61. In particular, the correlation between basin-wide denudation and k_{sn} suggests that the n
495 parameter of the stream power model can be approximated to 1, as typically observed in slow tectonic
496 settings, where basin-averaged slope and k_{sn} are usually lower than 25° and 200 $m^{0.9}$, respectively
497 (Fig. S4). Finally, the basin-wide denudation rates are insensitive to averaged annual precipitation
498 rates (Fig. 8d), testifying the lack of a clear dependency of denudation processes to precipitation, as

499 also observed in other slow tectonic ranges characterized by different climatic conditions (Fig. S4;
500 Burbank and Anderson, 2003; Godard et al., 2019; Clementucci et al., 2022).

501

502 **5.3.Topographic evolution and uplift history**

503 The axial zone of the WMM was likely above sea level before the Lutetian (early Cenozoic / middle
504 Eocene) as suggested by the lack of Eocene sediments (Phosphate Plateau), which can be found only
505 along its periphery (Er Rbia Basin) where the phosphatic series shows a deepening and thickening
506 south-westward trend (Fig. 9a; El Kiram et al., 2019). This sedimentation pattern indicates that, while
507 western Morocco was locally subjected to Eocene subsidence and marine sedimentation, the WMM
508 was affected by different processes (Charton et al., 2020). In addition, ~ 200- to 270-Myr-old apatite
509 fission track cooling ages and associated thermal histories indicate limited vertical movements since
510 the Triassic and suggest that the relict landscape might have started to form even earlier than the
511 Lutetian, possibly from the latest Cretaceous (Barbero et al., 2010; Charton et al., 2020). Our inverted
512 rock uplift rates for the oldest resolved time interval (35-22 Ma) of 10-20 m/Myr are in the same
513 order of magnitude as the ^{10}Be-derived denudation rates averaged over 50 ka (Table 1) and the lava
514 incision rates averaged over the last 1 Ma (see U_1 in Fig. 10a), both for the relict landscape, and the
515 exhumation rates averaged over the last 70 Ma. The occurrence of similar modelled rock uplift and
516 denudation/incision rates across different time scales, could indicate the persistence of a long-term
517 balance between rock uplift and denudation (*i.e.*, steady state denudation; *e.g.,* Whipple, 2001; Willett
518 and Brandon, 2002). However, this observation is based on the overall patterns of denudation at
519 different time scales and does not consider short-term climate fluctuations, which usually precludes
520 the attainment of steady-state conditions over time, possibly triggering rapid changes in denudation
521 rates (Whipple, 2001; Champagnac et al., 2014).

522 Our fluvial inversion results indicate that in the WMM domain, the onset of uplift and associated
523 headward migration of the knickpoints likely started at about 22 Ma and continued until ~10 Ma, with

524 rates ranging from 30 to 50 m/Myr (see U_2 in Fig. 10b). This range of rock uplift rates falls also within
525 the range of ^{10}Be-derived denudation rates and lava flow incision rates downstream of major non-
526 lithological knickpoints (E_2 = 35-55 m/Myr, Figs. 9a and 10b). Barcos et al. (2014) described a
527 maturity stage of the Sebou Basin through a stream length-gradient analysis, which can be a sign of
528 the partial re-equilibrium of these basins since this early Miocene perturbation (Fig. 10b). These
529 portions of the landscape are still eroding at rates that could be representative of the uplift rate U_2
530 (Fig. 10b). Thus, our inverted rates suggest that the entire WMM started to be uplifted from 22-20
531 Ma, in agreement with the occurrence of uplifted Eocene marine deposits in the WMM and in the
532 axial zone of the FMA and coeval with the onset of Miocene alkaline volcanism (Fig. 10b; Salvan,
533 1954; El Kiram et al., 2019; El Attmani et al., 2021). Early Miocene uplift initiation could be also
534 coeval with the onset of widespread contractional deformation in the FMA (Gomez et al., 1996;
535 1998), in the High Atlas Mountains (El Harfi et al., 2001; Lanari et al., 2020a; 2020b) and in the Rif
536 mountains (Fig. 10b; Abbassi et al., 2020). At the same time, the southward migration of the Rifian
537 frontal thrust produced foreland subsidence with the deposition of unconformable marine deposits in
538 the South Rifian Corridor (Saiss and Skoura Basins; Fig. 10b; Capella et al., 2018). Particularly, the
539 Skoura Basin contains a Messinian shallow-water marine sequence possibly deposited in a gulf
540 bunded by the TMA and FMA (Babault et al., 2008; Capella et al., 2018). In the northern Middle
541 Atlas and the Rif Belt, uplift started sometime after 5-7 Ma (Charriere and Saint-Martin, 1989;
542 Babault et al., 2008) at rates of 170-220 m/Myr as testified by the modern elevation of the Messinian
543 deposits of the Skoura Basin and the closure of the marine South Rifian Corridor (Krijgsman et al.,
544 1999; Babault et al., 2008). This episode of more recent regional uplift was accompanied by a Plio-
545 Quaternary peak in volcanism (Fig. 1) and is also registered by the Western Meseta fluvial network
546 (Fig. 10c). There, our inferred rock uplift rates for the last 5-6 Ma increase up to 35 m/Myr (see U_3
547 in Fig. 10c). Thus, our modelling rates appear to document a two-stage uplift history of the WMM
548 that includes uplift initiation at 22-20 Ma (with maximum rates reached at about 15 Ma) followed by
549 a second pulse at 5-6 Ma.

Alternatively, the WMM, could have shared an uplift history like that one recorded by the uplifted marine sediment of the Skoura and Saiss Basins (Babault et al., 2008). This implies that the highest knickpoints bounding the elevated relict landscape were originated during the regional 5- to 7-My-old uplift phase (Babault et al., 2008). Although our linear inversion model is calibrated for ^{10}Be data, which integrates erosion rates for the last tens 50.000 years, there are strong indications that short- and long-term, thermochronologically derived, exhumation rates from the relict landscape for the Cenozoic are similar (Barbero et al., 2010). This is also valid for the denudation rates downstream of the most elevated knickpoints, which are consistent with the incision rates inferred from the lava flows over the last 1 Ma. Thus, we can conclude that our inversion is likely not biased by the time scale of the ^{10}Be rates. Moreover, if we apply the approach of profile reconstruction for estimating the timing of the increase in uplift rates, for a surface uplift of 415+- 55 m (Fig. 7), an erosion rate for the relict landscape up to 20 m/Ma and an uplift (equal to erosion) rate downstream of the knickpoint of 40-50 m/Ma (Fig. 8) we would expect an minimum onset of uplift between 13 and 20 Ma (see equation in figure 5 of Kirby and Whipple 2012). These estimates indicate that the uplift rates downstream of the relict landscape are too low to be consistent with a Messinian onset of surface uplift. Thus, the uplift in WMM should have started earlier than 7 Ma. Taken together, these observations suggest that the WMM and the northern sectors of the FMA, where the Skoura Basin is located, did not share the same uplift history pre 7 Ma. Consequently, a two-stage uplift history for the WMM appears to be the most likely scenario.

5.4. Implications for uplift mechanisms

The northern sector of Atlas-Meseta system displays a shorter (10-50 km) and longer (>100 km) wavelength topography associated with processes operating at crustal and deeper scale, respectively (Fig. 11; Gomez et al., 1998; Boulton et al., 2014; Miller et al., 2015; Pastor et al., 2015). In particular, the WMM consists of a NE-SW oriented, ~ 130 x 260 km, ~1500-m-high, topographic swell devoid

575 of Cenozoic deformation (Frizon de Lamotte et al., 2009; Barbero et al., 2010). Barbero et al. (2010)
576 interpreted the WMM as an open, lithospheric-scale fold that formed in response of shortening
577 processes (*i.e.*, lithospheric buckling). Although this mechanism has been documented for specific
578 rheological settings (*e.g.*, Cloetingh and Burov 2011), there are no geophysical data proving
579 lithospheric folding in the WMM. Alternative mechanisms which could explain the absence of crustal
580 deformation in the WMM and the occurrence of uplift with a topographic wavelength of a several
581 tens of km (up to more than 100 km) is the emplacement of igneous intrusion or magma underplating
582 (*e.g.*, Thybo and Artemieva, 2013; Townsend, 2022) and the removal of mantle lithosphere
583 (delamination; *e.g.*, Garzione et al., 2006; Göğüş, and Pysklywec, 2008).

584 Following the scenario constrained by our river-profile inversions, the uplift in the WMM started at
585 ~22-20 Ma, shortly before the onset of alkaline volcanism (~16 Ma; El Azzouzi et al., 2010; Fig. 9)
586 and up to 15 Myr earlier than the rise of the northern sectors of the FMA and the South Rifian Corridor
587 (5-7 Ma; Krijgsman et al., 1999; Babault et al., 2008; Fig 10). These observations suggest that uplift
588 in the WMM would predate the more recent regional uplift and the increase in uplift rates observed
589 at 22-20 Ma must be ascribed to localized processes. The cumulative surface uplift in the WMM is
590 ~415 m with uplift rates varying from 35 to 55 m/Myr during the middle Miocene, and ~30 m/Myr
591 over the last 5-6 Ma (Figs. 9 and 10). These rates indicate that the amount of rock uplift in the last 5-
592 6 Ma would correspond to ~150-180 m. If we consider steady constant denudation of the relict
593 landscape at ~15 m/Myr, the resulting surface uplift during the last 6 Ma will be ~90 m (180 – 90 m,
594 where 90 m is the surface lowering over the last 6 Ma at 15 m/Myr). Thus, accounting for all the
595 above considerations the cumulative surface uplift pre-6 Ma would be 325 m (415 – 90 m). Assuming
596 that Airy isostasy is maintained and considering 2.8 x 10^3 and 3.23 x 10^3 kg/m^3 as mean crustal (ρc)
597 and asthenospheric mantle (ρa) density respectively, a ~2000-m-thick intrusion will generate ~300 m
598 of surface uplift (note that $(\rho a - \rho c)/\rho c$ is the ratio between elevation gain and crustal thickening;
599 Turcotte and Schubert, 2002). Similarly, if we assume Airy isostasy and a density of the lithospheric
600 mantle (ρm) of 3.3* 10^3 kg/m^3 the same magnitude of surface uplift will be generated by the removal

601 of a ~14-km-thick blob of mantle (note that $(\rho m - \rho a)/\rho a$ is the ratio between elevation gain and
602 thickness of the removed lithospheric mantle; Molnar and Stock, 2009). A similar magnitude of
603 surface uplift (~500 m) has been also documented for the HP, although timing, rates and mechanism
604 of uplift are unknown (Fig. 11; Pastor et al., 2015).

605 In the FMA the topographic growth reflects the combination of deep-seated and crustal shortening
606 and thickening processes, that led to a cumulative surface uplift of about 1200 m as documented by
607 the river projections from the eastern FMA (Fig 11). Although we do not know the timing of this
608 surface uplift, the same magnitude of uplift occurred in the northern FMA during the last ~5-7 Ma as
609 documented by the uplifted, Messinian marine deposits of the Skoura Basin that are in unconformity
610 over folded Mesozoic limestones (Babault et al., 2008). Thus, it is reasonable to assume that most of
611 the 1200 m of surface uplift in the entire FMA, were gained between 5-7 Ma and the present day.
612 Recent surface uplift is also visible in the southern Rifian Corridor (Saiss and Taza-Guercif basins)
613 where marine sediments experienced ~850 m of surface uplift during the last 6-8 Ma (Krijgsman et
614 al., 1999; Babault et al., 2008). Overall, this configuration suggests that the northern FMA is
615 characterized by a complex long-term history of deformation, uplift, and subsidence predating the
616 last pulse of uplift, which produced ~1200 m of elevation gain at rates of ~170-220 m/Myr (Fig. 10).
617 This renewed uplift is almost coeval with the major, second phase of volcanism centred in the Middle
618 Atlas Mountains (Missenard et al., 2006; El Azzouzi et al., 2010) and could reflect large-scale
619 processes coupled with the reactivation of older tectonic structures (Frizon de Lamotte et al., 2009;
620 Babault et al., 2008) and possibly with the injection of large magmatic bodies within the crust.

621 Specifically, if we assume that shortening produced crustal thickening and surface uplift without
622 surface erosion and/or sediments deposition while Airy isostasy was approximately maintained,
623 thrusting in the FMA would have produced a surface elevation gain of 150 to 730 m over the last 7
624 Ma at rates of 20 to 100 m/Myr (Garzione et al., 2006; see equations and assumptions in Table 2).
625 The assumption of no erosion (or very limited and hence neglectable erosion) over the last 7 Ma is

626 justified by the occurrence of the well-preserved, uplifted, marine deposits. This increase in elevation
627 would correspond to a crustal thickening of 0.8 to 4.0 km, and if we assume an initial crustal thickness
628 of 28-32 km, we will expect a ~29- to 36.7-km-thick crust (Table 2). These predictions agree with
629 crustal thickness estimates obtained by Gomez et al. (1999) and Miller and Backer (2014; Fig. 11).
630 Consequently, the remaining 470-1050 m of surface uplift should reflect deep-seated processes (*i.e.,*
631 mantle driven) at uplift rates of 65-150 m/Myr.

632 These simple calculations indicate two possible end-member scenarios for the topographic growth of
633 the FMA during the last 5-7 Ma: 1) shortening was the main cause of surface uplift (730 m), which
634 occurred at ~100 m/Myr, while dynamic uplift (470 m) took place at ~65 m/Myr; 2) shortening
635 accounted for a smaller fraction of elevation gain (150 m) and led to uplift at ~20 m/Myr, while
636 dynamic uplift (1050 m) took place at ~150 m/Myr (Table 2). In both cases magma addition may
637 have also, at least locally, influenced to the topographic growth of the FMA, although it is not possible
638 to isolate such a contribution. In any case, if we consider that the volcanic lavas younger than 4 Ma
639 crossing major faults are undeformed, and that the marine deposits of the Skoura Basin are only
640 slightly tilted (< 10°), the amount of shortening and thickening during the Plio-Quaternary should be
641 marginal (El Azzouzi et al., 2010; Babault et al., 2008). Thus, the dynamic-supported scenario (option
642 2) seems to be the most reliable possibility (Fig. 10c profile 2) for the topographic growth of the FMA
643 (Babault et al., 2008).

644 Finally, the spatial pattern of surface and uplift rates over the last 5-7 Ma, document a large-scale
645 topographic bulge (wavelength > 300 km) centred in the FMA (Fig. 11). In this configuration, the
646 WMM appears to represent the western shoulder of a bulge with uplift at rates that are 2.5 to 6 times
647 lower than those inferred from the central bulge (Figs. 10c and 11b). This large wavelength signal
648 can be explained as results of lithospheric delamination/dripping or upwelling of asthenospheric
649 mantle associated with even deeper processes like the rise of plumes possibly sourced from the
650 Canary hotspot, or a combination of both (Duggen et al., 2009; Miller and Becker, 2014; Miller et

al., 2015). Although a large number of geophysical studies robustly detected a shallow LAB and Moho beneath the Middle Atlas, the nature of the regional, deep dynamic processes is still under debate (*e.g.*, Missenard et al., 2006; Clementucci et al., 2023). Given the wavelength and the amplitude of the most recent uplift event and the characteristics of coeval volcanism, we tend to favour the plume hypothesis. Dynamic rising of asthenospheric mantle can reconcile the occurrence of large-scale surface uplift, non-isostatically compensated topography, anomalous thinning of the crust and lithospheric mantle and intermittent Mio-pliocene alkaline volcanism.

In essence, we conclude that the regional topographic evolution of the northern Atlas-Meseta system can result from the contribution of deep components (plume activity and mantle lithospheric delamination) coupled with smaller-scale processes such as possible injection of magmatic bodies within the crust and crustal shortening and thickening, at least for the structural domains characterized by contractional deformation (*e.g.*, Middle and High Atlas).

6. Conclusion

Our study allows the characterisation of the magnitude, timing, and rates of the long-term topographic evolution of the northern domains of the Atlas-Meseta system. The preserved relict landscape standing at a high elevation and the occurrence of deeply incised valleys downstream of major non-lithological knickpoints document a transience in topography and hence different stages of topographic evolution. Specifically, the ancient relict topography displays low relief, slope, and k_{sn} values in association with low rates of denudation on both bedrock and watersheds (from 4 to 20 m/Myr). Conversely, the downstream portion of the landscape exhibits higher topographic metrics and denudation rates (up to 40 m/Myr) in response to an increase in rock uplift rate that led to a topographic rejuvenation. Within this general trend a few exceptions emerge. In certain catchments of the Western Meseta, the granite massifs exposed on top of the relict landscape provide a higher

675 amount of quartz than the downstream metamorphics, resulting in a mixed signal of ^{10}Be
676 concentration, giving lower denudation rates than expected. These findings highlight that the uneven
677 distribution of quartz-bearing rocks in the sampled catchments and their relative location within the
678 topographic sectors (*i.e.,* relict vs rejuvenated landscape) represent a critical point for deriving basin-
679 wide denudation rates.

680 Combined with geological data, our river-profile inversion results suggest that the elevated relict
681 surfaces of the WMM have been forming since the Eocene. Moreover, our inverted uplift rates
682 indicate that surface uplift and associated knickpoints migrations started at ~22-20 Ma and reached
683 peak values of ~55 m/Myr at ~15 Ma, while the relict portion of the WMM has been eroding steadily
684 at an average of 15 m/Myr. These values agree with our basin-wide denudation and fluvial incision
685 rates derived from 1-Myr-old lava flows for the relict landscape and the catchment area downstream
686 of non-lithological knickpoints. This Miocene uplift (first uplift phase) of the WMM led to a
687 cumulative surface uplift of ~400 m over a extent of ~ 130 x 260 km, and is interpreted to reflect
688 crustal-scale processes such as igneous intrusion or magma underplating.

689 Subsequently, from 5-7 Ma, regional uplift occurred as documented by uplifted, Messinian marine
690 deposits of the Skoura and Saiss basins and minor knickpoints over the WMM domain. Surface uplift
691 inferred from the modern elevation of these marine deposits in the northern FMA (Skoura Basin) is
692 ~1200 m, that agree also with estimates from the western FMA obtained from the river projections.
693 The larger scale (wavelength > 200 km) and the higher magnitude of uplift suggest that mantle
694 processes like upwelling of deep asthenospheric mantle (*i.e.*, plume) may have driven the topographic
695 rejuvenation of the entire Atlas-Meseta system including the WMM (second uplift phase). Uplift
696 occurred at rates ranging from of ~30 to ~170 m/Myr from the WMM to the FMA over a pattern
697 describing a bulge centred in the FMA, where the Plio-Quaternary volcanisms is also centred. The
698 WMM represents the western shoulder of this bulge. Finally, minor crustal thickening induced by
699 shortening may have also contributed to the post 7-Ma topographic growth of the FMA. Overall,

these results suggest that uplift in the WMM may have occurred in two major steps at 22-20 and 5-6 Ma, while in the FMA, at least in its northern and western sectors, the major uplift pulse occurred during the last 5-7 Ma.

Acknowledgments

This study is part of the PhD thesis of RC at the University of Roma Tre (PhD Cycle XXXIV). It was supported by the PhD School of Roma Tre and grant "Vinci 2020" awarded to RC (Number: C2-1403). PB was supported by the MIUR (Ministry of Education University and Research), Excellence Department Initiative, Art. 1, com. 314-337, Low 232/2016. The ASTER (CEREGE, Aix-en-Provence) AMS national facility, is supported by the INSU/CNRS, the ANR (Projets thématiques d'excellence programme for the Equipements d'Excellence) and the IRD. We thank G. Aumaître, K. Keddadouche and F. Zaidi for their expertise in AMS measurements, A. Yaaqoub, A. Essaifi, N. Youbi, A. Abbassi and R. Braucher for the stimulating discussions. We are indebted to P-H Blard, S. Willett and T. Schildgen for revising this manuscript as a chapter of the PhD Thesis of the first author, to J. Babault, G. Rixhon and anonymous Reviewers for the excellent and detailed revisions, to the Editor M. Stokes for managing the submission of the manuscript. Finally to L. Benedetti, M. Della Seta, P. Molin and O. Bellier for providing valuable comments during the PhD defense of RC.

References

Abbassi, A., Cipollari, P., Zaghloul, M. N., Cosentino, D., 2020. The Rif Chain (northern Morocco) in the late Tortonian-early Messinian tectonics of the Western Mediterranean orogenic belt: Evidence from the Tanger-Al Manzla wedge-top basin. Tectonics. 39(9). https://doi.org/10.1029/2020TC006164.

Abbassi, A., Cipollari, P., Fellin, M. G., Zaghloul, M. N., Guillong, M., El Mourabet, M., & Cosentino, D. (2022). The Numidian sand event in the Burdigalian foreland basin system of the Rif, Morocco, in a source-to-sink perspective. GSA Bulletin, 134(9-10), 2280-2304. https://doi.org/10.1130/B36136.1.

Adams, B. A., Whipple, K. X., Forte, A. M., Heimsath, A. M., & Hodges, K. V. 2020. Climate controls on erosion in tectonically active landscapes. Sci. adv. 6(42), eaaz3166. https://www.science.org/doi/10.1126/sciadv.aaz3166.

Agharroud, K., Siame, L. L., Ben Moussa, A., Bellier, O., Guillou, V., Fleury, J., and El Kharim, Y. (2021). Seismo-tectonic model for the southern Pre-Rif border (Northern Morocco): Insights from morphochronology. Tectonics. 40(4), e2020TC006633. https://doi.org/10.1029/2020TC006633.

Arboleya, M. L., Teixell, A., Charroud, M., Julivert, M., 2004. A structural transect through the High and Middle Atlas of Morocco. J. Afr. Earth. Sci. 39(3-5), 319-327. https://doi.org/10.1016/j.jafrearsci.2004.07.036.

Babault, J., Teixell, A., Arboleya, M. L., Charroud, M., 2008. A Late Cenozoic age for long-wavelength surface uplift of the Atlas Mountains of Morocco. Terra nova. 20(2), 102-107. https://doi.org/10.1111/j.1365-3121.2008.00794.x.

Babault, J., Van Den Driessche, J., and Charco, M., 2022, 2.10 - Plateau Uplift, Regional Warping, and Subsidence, in Shroder, J. F., ed., Treatise on Geomorphology (Second Edition): Oxford, Academic Press, p. 223-269. https://doi.org/10.1016/B978-0-12-818234-5.00119-X.

Balco, G., Stone, J. O., Lifton, N. A., Dunai, T. J., 2008. A complete and easily accessible means of calculating surface exposure ages or erosion rates from 10Be and 26Al measurements. Quat. Geochronol. 3(3), 174-195. https://doi.org/10.1016/j.quageo.2007.12.001.Ballato, P., Landgraf, A., Schildgen, T. F., Stockli, D. F., Fox, M., Ghassemi, M. R., Kirby, E., Strecker, M. R., 2015. The growth of a mountain belt forced by base-level fall: Tectonics and surface processes during the evolution of the Alborz Mountains, N Iran. Earth and Planet. Sci. Lett. 425, 204-218. https://doi.org/10.1016/j.epsl.2015.05.051.

Barbero, L., Jabaloy, A., Gómez-Ortiz, D., Pérez-Peña, J. V., Rodríguez-Peces, M. J., Tejero, R., Estupinan, J., Azdimousa, A., Vazquez, M., Asebriy, L., 2011. Evidence for surface uplift of the Atlas Mountains and the surrounding peripheral plateaux: Combining apatite fission-track results and geomorphic indicators in the Western Moroccan Meseta (coastal Variscan Paleozoic basement). Tectonophysics. 502(1-2), 90-104. https://doi.org/10.1016/j.tecto.2010.01.005.

Borchers, B., Marrero, S., Balco, G., Caffee, M., Goehring, B., Lifton, N., Nishiizumi, K., Phillips, F., Schaefer, J., Stone, J., 2016. Geological calibration of spallation production rates in the CRONUS-Earth project. Quat. Geochronol. 31, 188–198. https://doi.org/10.1016/j.quageo.2015.01.009.

Boulton, S. J., Stokes, M., & Mather, A. E. (2014). Transient fluvial incision as an indicator of active faulting and Plio-Quaternary uplift of the Moroccan High Atlas. Tectonophysics, 633, 16-33.https://doi.org/10.1016/j.tecto.2014.06.032.

763 Braucher, R., Merchel, S., Borgomano, J., Bourlès, D. L., 2011. Production of cosmogenic
764 radionuclides at great depth: A multi element approach. Earth Planet. Sci. Lett. 309(1-2), 1-9.
765 https://doi.org/10.1016/j.epsl.2011.06.036.
766 Burbank, D. W., and Anderson, R. S., 2009. Tectonic geomorphology. John Wiley & Sons.
767 https://doi.org/ 10.1002/9781444345063.
768 Calvet, M., Gunnell, Y., Farines, B., 2015. Flat-topped mountain ranges: Their global distribution
769 and value for understanding the evolution of mountain topography. Geomorphology. 241, 255-
770 291. https://doi.org/10.1016/j.geomorph.2015.04.015.
771 Capella, W., Barhoun, N., Flecker, R., Hilgen, F. J., Kouwenhoven, T., Matenco, L. C., Sierro L.C.,
772 Tulbure, M.A., Yousfi, M.Z., and Krijgsman, W., 2018. Palaeogeographic evolution of the
773 late Miocene Rifian Corridor (Morocco): reconstructions from surface and subsurface data.
774 Earth-Science Reviews, 180, 37-59.
775 Carretier, S., Regard, V., Vassallo, R., Martinod, J., Christophoul, F., Gayer, E., Audin L., Lagane,
776 C., 2015. A note on 10Be-derived mean erosion rates in catchments with heterogeneous
777 lithology: Examples from the western Central Andes. Earth Surf. Processes Landforms.
778 40(13), 1719-1729. https://doi.org/10.1002/esp.3748.
779 Champagnac, J. D., Valla, P. G., & Herman, F., 2014. Late-Cenozoic relief evolution under evolving
780 climate: A review. Tectonophysics. 614, 44-65. https://doi.org/10.1016/j.tecto.2013.11.037
781 Charriere, A. and Saint-Martin, J.P., 1989. Relations entre les formations re´cifales du Miocene
782 superieur et la dynamique d'ouverture et de fermeture des communications marines a la
783 bordure me´ridionale du sillon sud-rifain (Maroc). C. R. Acad. Sci. II, 309, 611–614.
784 Charriere, A., 1984. Évolution néogène de bassins continentaux et marins dans le Moyen Atlas central
785 (Maroc). Bull. Soc. Géol. Fr. 7(6), 1127-1136.
786 Charton, R., Bertotti, G., Arnould, A. D., Storms, J. E., and Redfern, J., 2021. Low-temperature
787 thermochronology as a control on vertical movements for semi-quantitative source-to-sink
788 analysis: A case study for the Permian to Neogene of Morocco and surroundings. Basin
789 Research, 33(2), 1337-1383. https://doi.org/10.1111/bre.12517.
790 Chmeleff, J., von Blanckenburg, F., Kossert, K., Jakob, D., 2010. Determination of the 10Be half-life
791 by multicollector ICP-MS and liquid scintillation counting. Nucl. Instrum. Methods Phys.
792 Res., Sect. B, Beam Interact. Mater. Atoms. 268(2), 192–199.
793 https://doi.org/10.1016/j.nimb.2009.09.012.
794 Clementucci, R., 2022. Deciphering mantle contribution on surface uplift in the Atlas-Meseta system
795 (Morocco) (Doctoral dissertation). Earth Sciences. Università degli studi Roma Tre; Aix
796 Marseille Univ. https://tel.archives-ouvertes.fr/tel-03630297/document.

Clementucci R., Ballato P., Siame L., Faccenna C., Yaaqoub A., Essaifi A., Leanni L., Guillou V., 2022. Lithological control on topographic relief evolution in a slow tectonic setting (Anti-Atlas, Morocco). Earth and Planet. Sci. Lett. https://doi.org/10.1016/j.epsl.2022.117788.

Clementucci, R., Ballato, P., Siame, L., Fox, M., Lanari, R., Sembroni, A., Faccenna, C., Yaaqoub, A., Essaifi, A., (2023). Surface uplift and topographic rejuvenation of a tectonically inactive range: Insights from the Anti-Atlas and the Siroua Massif (Morocco). Tectonics. 42, e2022TC007383. https://doi.org/10.1029/2022TC007383Cloetingh, S., and Burov, E., 2011. Lithospheric folding and sedimentary basin evolution: a review and analysis of formation mechanisms. Basin Research, 23(3), 257-290. https://doi.org/10.1111/j.1365-2117.2010.00490.x.

Crosby, B. T., and Whipple, K. X., 2006. Knickpoint initiation and distribution within fluvial networks: 236 waterfalls in the Waipaoa River, North Island, New Zealand. Geomorphology. 82(1-2), 16-38. https://doi.org/10.1016/j.geomorph.2005.08.023.

Duggen, S., Hoernle, K. A., Hauff, F., Kluegel, A., Bouabdellah, M., Thirlwall, M. F., 2009. Flow of Canary mantle plume material through a subcontinental lithospheric corridor beneath Africa to the Mediterranean. Geology. 37(3), 283-286. https://doi.org/10.1130/G25426A.1.

El Attmani, M., Bouwafoud, A., Elouariti, S., Mhamdi, H. S., Bouziane, A. B., Mouflih, M., 2021. The Eocene Bryozoans of Bekrit-Timahdite Formation, Middle-Atlas, Morocco: Taxonomy, Paleoenvironments and Paleoclimates Implications. J. Geosci. Env. Prot. 9(3), 136-153. https://doi.org/10.4236/gep.2021.93008.

El Azzouzi, M. H., Maury, R. C., Bellon, H., Youbi, N., Cotten, J., Kharbouch, F., 2010. Petrology and K-Ar chronology of the Neogene-quaternary Middle Atlas basaltic province, Morocco. Bull. Soc. Géol. Fr. 181(3), 243-257. https://doi.org/10.2113/gssgfbull.181.3.243.

El Kiram, N., Jaffal, M., Kchikach, A., El Azzab, D., El Ghorfi, M., Khadiri, O., Jourani, E., Manar, A., and Nahim, M., 2019. Phosphatic series under Plio-Quaternary cover of Tadla Plain, Morocco: Gravity and seismic data. C. R. Geosci. 351(6), 420-429.

England, P., Molnar, P., 1990. Surface uplift, uplift of rocks, and exhumation of rocks. Geology. 18(12), 1173-1177. https://doi.org/10.1130/0091-7613(1990)018<1173:SUUORA>2.3.CO;2.

Faccenna, C., Becker, T. W., 2020. Topographic expressions of mantle dynamics in the Mediterranean. Earth-Science Reviews. 209, 103327. https://doi.org/10.1016/j.earscirev.2020.103327.

Fernandes, V. M., Roberts, G. G., White, N., & Whittaker, A. C., 2019. Continental-scale landscape evolution: A history of North American topography. J. Geophys. Res.,Earth Surface, 124(11), 2689-2722. https://doi.org/10.1029/2018JF004979.

Forte, A.M., Whipple, K.X., 2019. Short communication: the Topographic Analysis Kit (TAK) for TopoToolbox. Earth Surf. Dyn.7, 87–95. https://doi.org/10.5194/esurf-7-87-2019.

Frizon de Lamotte, D., Leturmy, P., Missenard, Y., Khomsi, S., Ruiz, G., Saddiqi, O., Guillocheau F., Michard A., 2009. Mesozoic and Cenozoic vertical movements in the Atlas system (Algeria, Morocco, Tunisia). An overview: Tectonophysics. 475, 9–28. https://doi.org/10.1016/j.tecto.2008.10.024.

Godard, V., Dosseto, A., Fleury, J., Bellier, O., Siame, L., ASTER Team., 2019. Transient landscape dynamics across the Southeastern Australian Escarpment. Earth and Planet. Sci. Lett. 506, 397-406. https://doi.org/10.1016/j.epsl.2018.11.017.

Gallen, S. F., Wegmann, K. W., 2017. River profile response to normal fault growth and linkage: An example from the Hellenic forearc of south-central Crete, Greece. Earth Surf. Dyn. 5(1), 161-186. https://doi.org/10.5194/esurf-5-161-2017.

Gallen, S. F., 2018. Lithologic controls on landscape dynamics and aquatic species evolution in post-orogenic mountains. Earth and Planet. Sci. Lett. 493, 150-160. https://doi.org/10.1016/j.epsl.2018.04.029.

Garzione, C. N., Molnar, P., Libarkin, J. C., MacFadden, B. J., 2006. Rapid late Miocene rise of the Bolivian Altiplano: Evidence for removal of mantle lithosphere. Earth and Planet. Sci. Lett. 241(3-4), 543-556. https://doi.org/10.1016/j.epsl.2005.11.026.

Gomez, F., Barazangi, M., Bensaid, M., 1996. Active tectonism in the intracontinental Middle Atlas Mountains of Morocco: synchronous crustal shortening and extension. J. Geol. Soc. 153(3), 389-402. https://doi.org/10.1144/gsjgs.153.3.0389.

Gomez, F., Allmendinger, R., Barazangi, M., Er-Raji, A., Dahmani, M., 1998. Crustal shortening and vertical strain partitioning in the Middle Atlas Mountains of Morocco. Tectonics. 17(4), 520-533. https://doi.org/10.1029/98TC01439.

Göğüş, O. H., Pysklywec, R. N., 2008. Near-surface diagnostics of dripping or delaminating lithosphere. J. Geophys. Res., Solid Earth. 113(B11). https://doi.org/10.1029/2007JB005123.

Goren, L., Fox, M., Willett, S. D., 2014. Tectonics from fluvial topography using formal linear inversion: Theory and applications to the Inyo Mountains, California. J. Geophys. Res. F: Earth Surf. 119(8), 1651-1681. https://doi.org/10.1002/2014JF003079.

Hoepffner, C., Soulaimani, A., Piqué, A., 2005. The moroccan hercynides. J. Afr. Earth. Sci. 43(1-3), 144-165. https://doi.org/10.1016/j.jafrearsci.2005.09.002.

Huffman, G. J., Bolvin, D. T., Braithwaite, D., Hsu, K., Joyce, R., Xie, P., & Yoo, S. H., 2015. NASA global precipitation measurement (GPM) integrated multi-satellite retrievals for GPM

(IMERG). Algorithm Theoretical Basis Document (ATBD) Version, 4, 26. http://pmm.nasa.gov/sites/default/files/document_files/IMERG_ATBD_V4.5.pdf.

Jolivet, L., & Faccenna, C., 2000. Mediterranean extension and the Africa-Eurasia collision. Tectonics. 19(6), 1095-1106. https://doi.org/10.1029/2000TC900018.

Kirby, E., Whipple, K. X., 2012. Expression of active tectonics in erosional landscapes. J. Struct. Geol. 44, 54-75. https://doi.org/10.1016/j.jsg.2012.07.009.

Korschinek, G., Bergmaierb, A., Faestermanna, T., Gerstmannc, U.C., Kniea, K., Rugela, G., Wallnerd, A., Dillmanna, I., Dollingerb, G., Lierse von Gostomskie, Ch., Kossertf, K., Maitia, M., Poutivtseva, M., Remmer, A., 2010. A new value for the half-life of 10Be by heavy ion elastic recoil detection and liquid scintillation counting. Nucl. Instr. Meth Res. B. https://doi.10.1016/j.nimb.2009.09.020. Krijgsman, W., Langereis, C. G., Zachariasse, W. J., Boccaletti, M., Moratti, G., Gelati, R., Iaccarino, F., Papani, G., Villa, G., 1999. Late Neogene evolution of the Taza–Guercif Basin (Rifian Corridor, Morocc\o) and implications for the Messinian salinity crisis. Mar. Geol. 153(1-4), 147-160. https://doi.org/10.1016/S0025-3227(98)00084-X.

Lal, D., 1991. Cosmic ray labeling of erosion surfaces: in situ nuclide production rates and erosion models. Earth Planet. Sci. Lett.104, 424–439. http://dx.doi.org/10.1016/0012-821X(91)90220-C

Lanari, R., Fellin, M. V., Faccenna, C., Balestrieri, M. L., Pazzaglia, F. J., Youbi, N., Maden, C., 2020a. Exhumation and surface evolution of the western high atlas and surrounding regions as constrained by low-temperature thermochronology. Tectonics. 39(3), e2019TC005562. https://doi.org/10.1029/2019TC005562.

Lanari, R., Faccenna, C., Fellin, M. G., Essaifi, A., Nahid, A., Medina, F. and Youbi, N., 2020b. Tectonic evolution of the western high Atlas of Morocco: oblique convergence, reactivation, and transpression. Tectonics, 39(3), e2019TC005563. https://doi.org/10.1029/2019TC005563.

Lanari, R., Reitano, R., Giachetta, E., Pazzaglia, F.J., Clementucci, R., Faccenna, C., Fellin, M.G., 2022. Is the Anti-Atlas of Morocco still uplifting? J. Afr. Earth Sci.188, 104481. https://doi .org /10 .1016 /j .jafrearsci .2022 .104481.

Lanari, R., Boutoux, A., Faccenna, C., Herman, F., Willett, S. D., & Ballato, P., 2023. Cenozoic exhumation in the Mediterranean and the Middle East. Earth-Science Reviews, 104328

Marder, E., & Gallen, S. F., 2023. Climate control on the relationship between erosion rate and fluvial topography. Geology. https://doi.org/10.1130/G50832.1.

Marra, F., Rohling, E. J., Florindo, F., Jicha, B., Nomade, S., Pereira, A., & Renne, P. R., 2016. Independent 40Ar/39Ar and 14C age constraints on the last five glacial terminations from the aggradational successions of the Tiber River, Rome (Italy). Earth and Planetary Science Letters, 449, 105-117. https://doi.org/10.1016/j.epsl.2016.05.037.

Meyer, H., Hetzel, R., Fügenschuh, B., Strauss, H., 2010. Determining the growth rate of topographic relief using in situ-produced 10Be: a case study in the Black Forest, Germany. Earth and Planet. Sci. Lett. 290(3-4), 391-402. https://doi.org/10.1016/j.epsl.2009.12.034

Miller, S. R., Sak, P. B., Kirby, E., Bierman, P. R., 2013. Neogene rejuvenation of central Appalachian topography: Evidence for differential rock uplift from stream profiles and erosion rates. Earth and Planet. Sci. Lett. 369, 1-12. https://doi.org/10.1016/j.epsl.2013.04.007.

Miller, M. S., Becker, T. W., 2014. Reactivated lithospheric-scale discontinuities localize dynamic uplift of the Moroccan Atlas Mountains. Geology. 42(1), 35-38. https://doi.org/10.1130/G34959.1.

Miller, M. S., O'Driscoll, L. J., Butcher, A. J., Thomas, C., 2015. Imaging Canary Island hotspot material beneath the lithosphere of Morocco and southern Spain. Earth and Planet. Sci. Lett. 431, 186-194. https://doi.org/10.1016/j.epsl.2015.09.026.

Miller, K. G., Browning, J. V., Schmelz, W. J., Kopp, R. E., Mountain, G. S., & Wright, J. D., 2020. Cenozoic sea-level and cryospheric evolution from deep-sea geochemical and continental margin records. Science advances, 6(20), eaaz1346. https://doi.org/10.1126/sciadv.aaz1346.

Missenard, Y., Zeyen, H., Frizon de Lamotte, D., Leturmy, P., Petit, C., Sébrier, M., Saddiqi, O., 2006. Crustal versus asthenospheric origin of relief of the Atlas Mountains of Morocco. J. Geophys. Res., Solid Earth. 111(B3). https://doi.org/10.1029/2005JB003708.

Olivetti, V., Godard, V., Bellier, O., and ASTER team., 2016. Cenozoic rejuvenation events of Massif Central topography (France): Insights from cosmogenic denudation rates and river profiles. Earth and Planet. Sci. Lett. 444, 179-191. https://doi.org/10.1016/j.epsl.2016.03.049.

Pastor, A., Babault, J., Owen, L. A., Teixell, A., Arboleya, M. L., 2015. Extracting dynamic topography from river profiles and cosmogenic nuclide geochronology in the Middle Atlas and the High Plateaus of Morocco. Tectonophysics. 663, 95-109. https://doi.org/10.1016/j.tecto.2015.06.007.

Pavano, F., & Gallen, S. F., 2021. A geomorphic examination of the Calabrian forearc translation. Tectonics, 40(7), e2020TC006692. https://doi.org/10.1029/2020TC006692.

Peifer, D., Persano, C., Hurst, M. D., Bishop, P., & Fabel, D., 2021. Growing topography due to contrasting rock types in a tectonically dead landscape. Earth Surface Dynamics. 9(2), 167-181. https://doi.org/10.5194/esurf-9-167-2021.

Perron, J. T., Royden, L., 2013. An integral approach to bedrock river profile analysis. Earth Surf. Processes Landforms. 38(6), 570-576. https://doi.org/10.1002/esp.3302.

Racano, S., Schildgen, T. F., Cosentino, D., Miller, S. R., 2021. Temporal and spatial variations in rock uplift from river-profile inversions at the Central Anatolian Plateau southern margin. J. Geophys. Res. F: Earth Surf. 126(8). https://doi.org/10.1029/2020JF006027.

Rachdi, H., 1995. Etude du volcanisme plio-quaternaire du Maroc central: pétrographie, géochimie et minéralogie. Notes Mém. Serv. Géol. Maroc. 381, 157.

Riebe, C. S., Kirchner, J. W., Finkel, R. C., 2004. Erosional and climatic effects on long-term chemical weathering rates in granitic landscapes spanning diverse climate regimes. Earth and Planet. Sci. Lett. 224(3-4), 547-562. https://doi.org/10.1016/j.epsl.2004.05.019.

Roberts, G. G., & White, N., 2010. Estimating uplift rate histories from river profiles using African examples. J. Geophys. Res., Solid Earth. 115(B2). https://doi.org/10.1029/2009JB006692.

Rosenkranz, R., Schildgen, T., Wittmann, H., Spiegel, C., 2018. Coupling erosion and topographic development in the rainiest place on Earth: Reconstructing the Shillong Plateau uplift history with in-situ cosmogenic ^{10}Be. Earth and Planet. Sci. Lett. 483, 39-51. https://doi.org/10.1016/j.epsl.2017.11.047.

Salvan, H., Farkhany, M., 1982. Les phosphates de chaux sédimentaires du Maroc. Leurs caractéristiques et leurs problèmes (essai de synthèse). Notes Mem. Serv. geol. Maroc 14, 7e20.

Schwanghart, W., Scherler, D., 2014. Short communication: TopoToolbox 2 – MATLAB-based software for topographic analysis and modeling in Earth surface sciences. Earth Surf. Dyn. 2, 1–7. https://doi.org/10.5194/esurf-2-1-2014.

Sembroni, A., Kiraly, A., Faccenna, C., Funiciello, F., Becker, T. W., Globig, J., & Fernandez, M., 2017. Impact of the lithosphere on dynamic topography: Insights from analogue modeling. Geophysical Research Letters, 44(6), 2693-2702. https://doi.org/10.1002/2017GL072668.

Sembroni, A., Molin, P., Soligo, M., Tuccimei, P., Anzalone, E., Billi, A., Franchini, S., Rinaldi, M., and Tarchini, L., 2020. The uplift of the Adriatic flank of the Apennines since the Middle Pleistocene: New insights from the Tronto River basin and the Acquasanta Terme Travertine (central Italy). Geomorphology, 352, 106990. https://doi.org/10.1016/j.geomorph.2019.106990.

Smith, A. G., Fox, M., Schwanghart, W., Carter, A., 2022. Comparing methods for calculating channel steepness index. Earth-Science Reviews, 227, 103970. https://doi.org/10.1016/j.earscirev.2022.103970.

964 Snyder, N. P., Whipple, K. X., Tucker, G. E., & Merritts, D. J., 2000. Landscape response to tectonic
965 forcing: Digital elevation model analysis of stream profiles in the Mendocino triple junction
966 region, northern California. Geological Society of America Bulletin, 112(8), 1250-1263.
967 https://doi.org/10.1130/0016-7606(2000)112<1250:LRTTFD>2.0.CO;2.
968 Snyder, N. P., Whipple, K. X., Tucker, G. E., Merritts, D. J., 2002. Interactions between onshore
969 bedrock-channel incision and nearshore wave-base erosion forced by eustasy and tectonics.
970 Basin Research. 14(2), 105-127. https://doi.org/10.1046/j.1365-2117.2002.00169.x.
971 Stokes, M., Mather, A. E., Belfoul, M., Faik, F., Bouzid, S., Geach, M. R., Cunha, P.P., Boulton, S.J.,
972 & Thiel, C. (2017). Controls on dryland mountain landscape development along the NW
973 Saharan desert margin: Insights from Quaternary river terrace sequences (Dadès River, south-
974 central High Atlas, Morocco). Quaternary Science Reviews, 166, 363-
975 379.https://doi.org/10.1016/j.quascirev.2017.04.017.
976 Townsend, M., 2022. Linking surface deformation to thermal and mechanical magma chamber
977 processes. Earth and Planet. Sci. Lett. 577, 117272.
978 https://doi.org/10.1016/j.epsl.2021.117272.
979 Turcotte, D. L., & Schubert, G., 2002. Geodynamics. Cambridge university press.
980 Vernant, P., Fadil, A., Mourabit, T., Ouazar, D., Koulali, A., Davila, J. M., Garate, J., McClusky, A.,
981 Reilinger, R., 2010. Geodetic constraints on active tectonics of the Western Mediterranean:
982 Implications for the kinematics and dynamics of the Nubia-Eurasia plate boundary zone.
983 Journal of Geodynamics. 49(3-4), 123-129. https://doi.org/10.1016/j.jog.2009.10.007.
984 Whipple, K. X., 2001. Fluvial landscape response time: How plausible is steady-state denudation?.
985 American Journal of Science, 301(4-5), 313-325. https://doi.org/10.2475/ajs.301.4-5.313.
986 Willett, S. D., & Brandon, M. T., 2002. On steady states in mountain belts. Geology. 30(2), 175-178.
987 https://doi.org/10.1130/0091-7613(2002)030<0175:OSSIMB>2.0.CO;2.
988 Wobus, C., Whipple, K. X., Kirby, E., Snyder, N., Johnson, J., Spyropolou, K., Crosby B., &
989 Sheehan, D., 2006. Tectonics from topography: Procedures, promise, and pitfalls. Special
990 Papers - Geological Society of America, 398, 55. https://doi.org/10.1130/2006.2398(04).
991 Yang, R., Willett, S. D., Goren, L., 2015. In situ low-relief landscape formation as a result of river
992 network disruption. Nature. 520(7548), 526-529. https://doi.org/10.1038/nature14354.
993 Zhong, Y., Willett, S. D., Picotti, V., Xiong, J., & Zhang, H., 2022. Spatial and temporal variations
994 of incision rate of the middle Yellow River and its tributaries. Journal of Geophysical
995 Research: Earth Surface, 127(1), e2021JF006327. https://doi.org/10.1029/2021JF006327.
996 Zondervan, J. R., Stokes, M., Boulton, S. J., Telfer, M. W., & Mather, A. E., 2020. Rock strength and
997 structural controls on fluvial erodibility: Implications for drainage divide mobility in a

collisional mountain belt. Earth and Planetary Science Letters, 538, 116221.https://doi.org/10.1016/j.epsl.2020.116221.

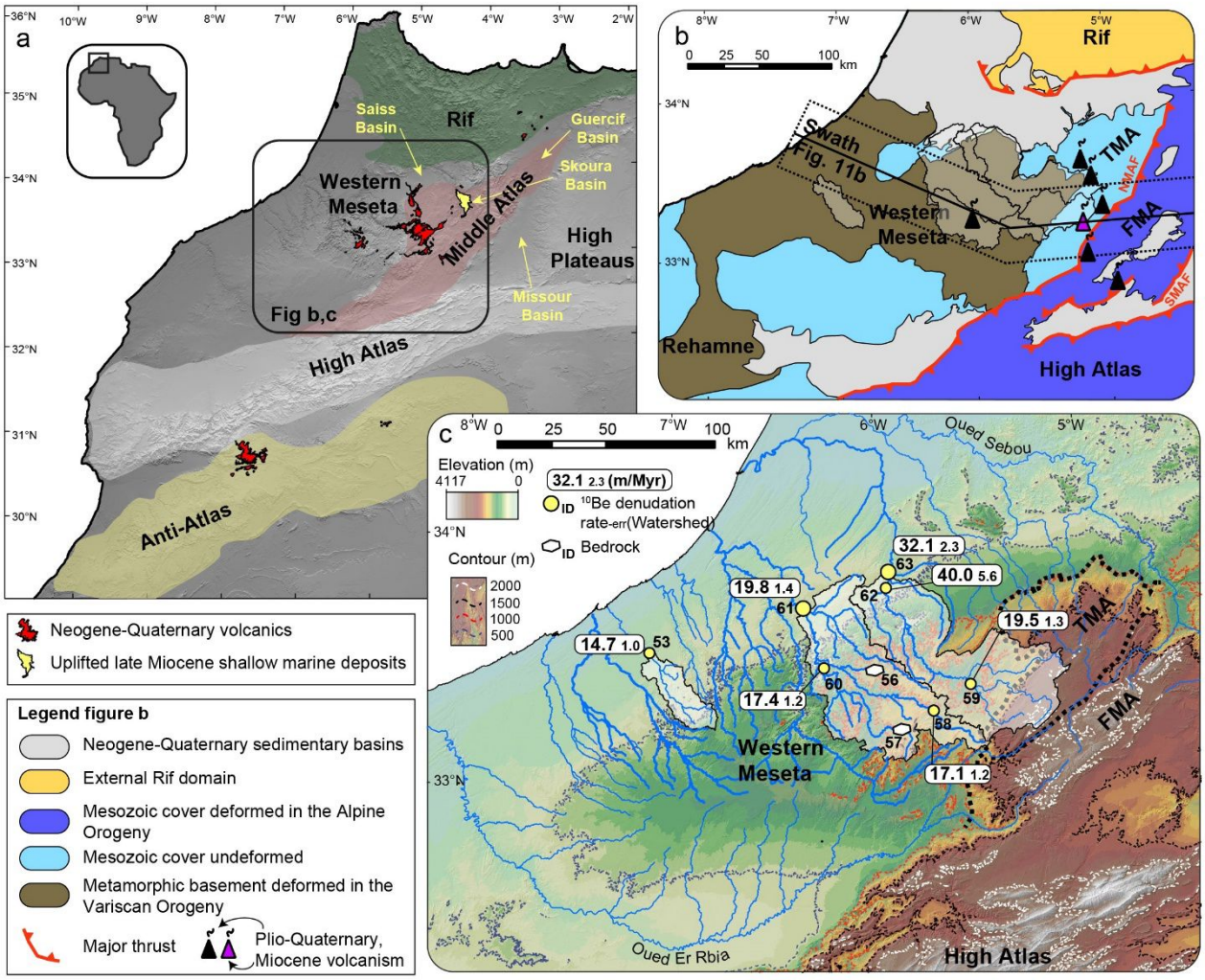

Figure 1. (a) Topographic hillshade of the Rif, Atlas and Meseta domains. **(b)** Morpho-structural domains in the western central Morocco and selected . FMA: Folded Middle Atlas. TMA: Tabular Middle Atlas. NMAF: North Middle Atlas fault. SMAF: South Middle Atlas fault. **(c)** DEM of the Western Moroccan Meseta. The white transparent areas show the sampled catchments while the dots show the location of the sampling points. Note the occurrence of two major catchment and several sub-catchments. The white hexagons show the location of bedrock samples. The thick dashed line indicates the boundary between the TMA, the FMA and the Western Meseta.

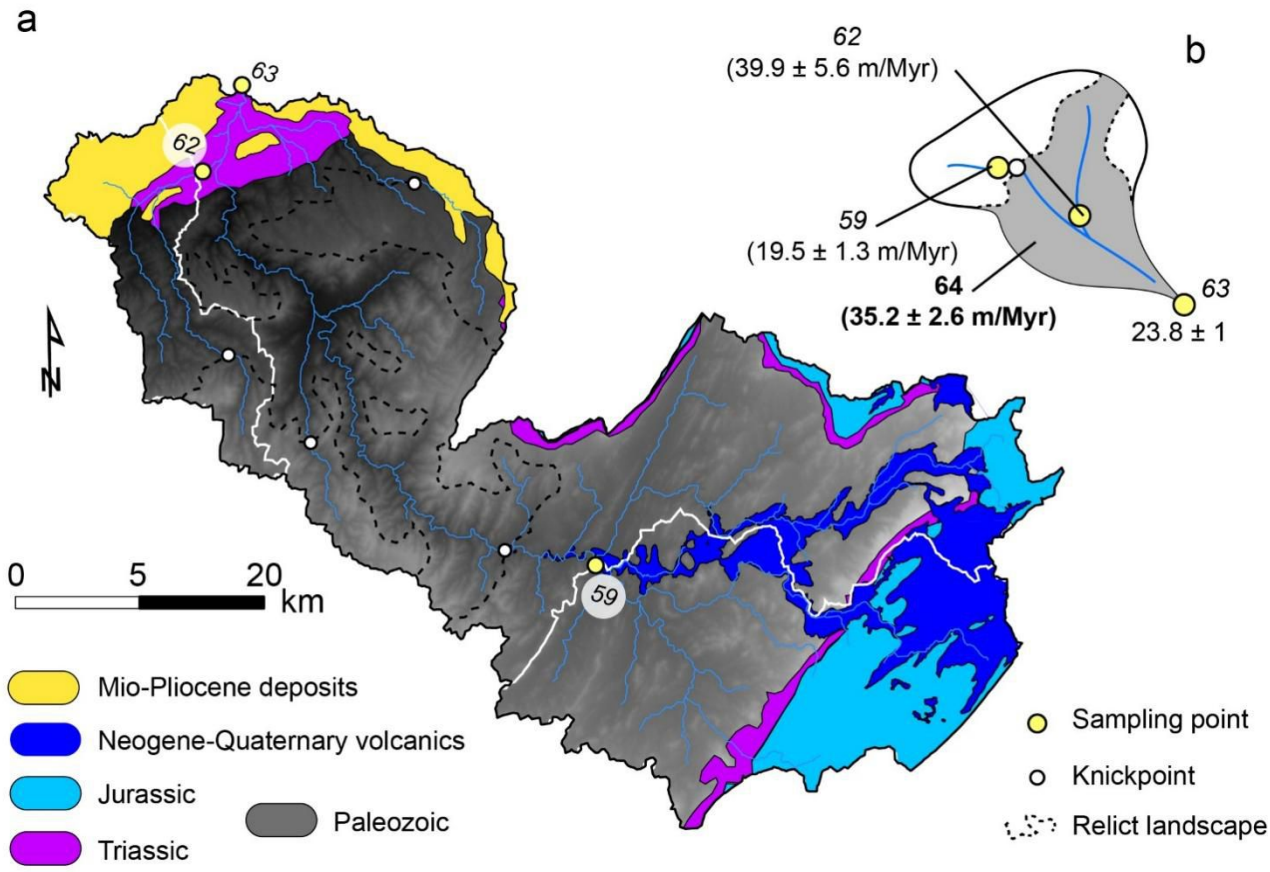

Figure 2. (a) Topographic and geological map of the sampled catchment 63. Note, sampling point 59 is located upstream the non-lithological knickpoint, 62 is downstream the non-lithological knickpoint and 63 represents the mixed rate of basin-wide denudation. **(b)** Schematic illustration of the catchment 63, showing the correction method to estimate the denudation rate of the downstream portion (64) of the catchment 63, by using drainage area and denudation rate of the basin 63 and 59, respectively. Note, basin-wide denudation derived from basin 62 is consistent with estimate value of the basin 64, both located in the downstream of non-lithological knickpoints.

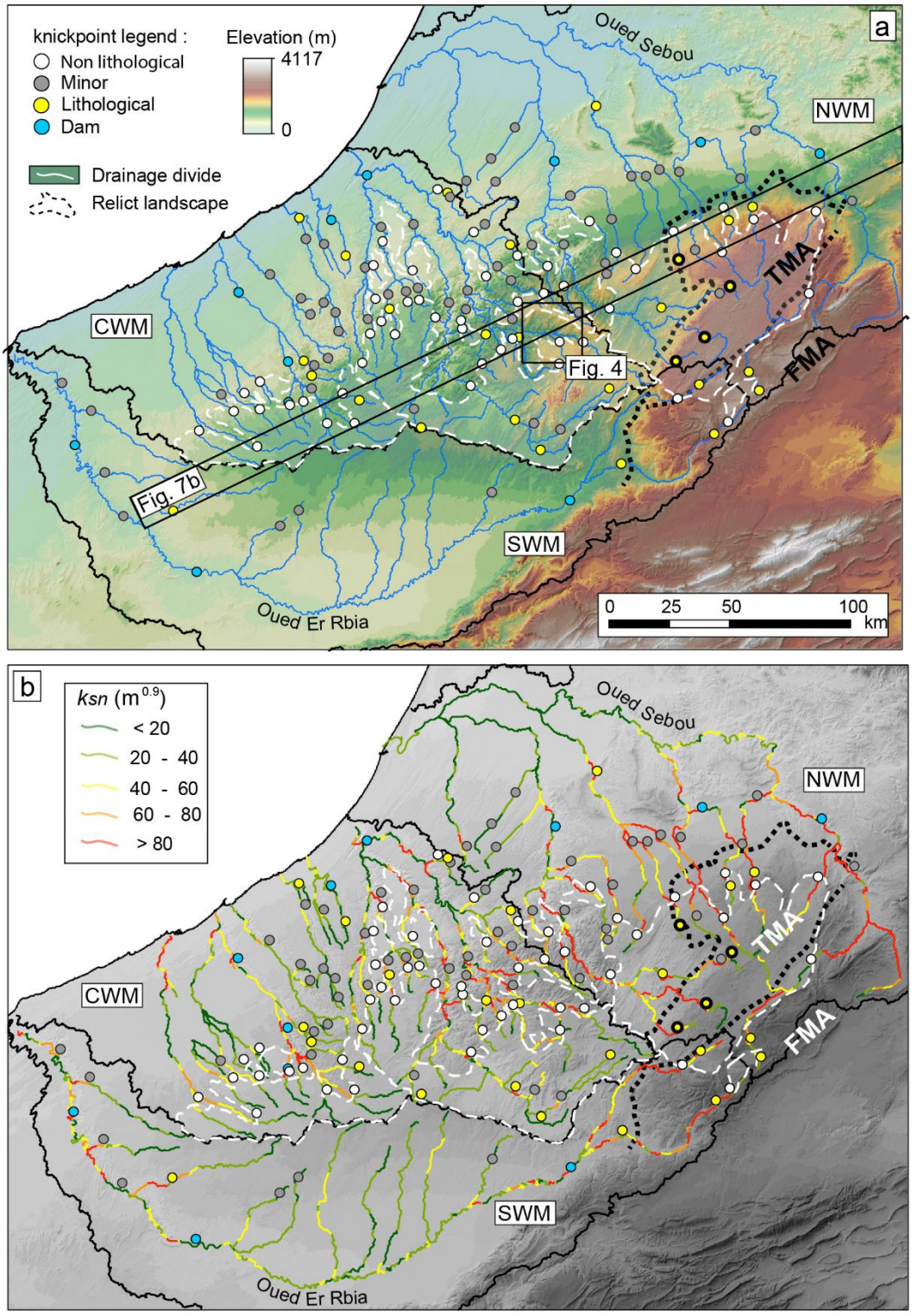

Figure 3. (a) DEM **(b)** k_{sn} map with main knickpoints. The bold knickpoints demark the escarpment between the TMA and Western Moroccan Meseta (WMM), while the thick dashed line indicates the boundary between the main morpho-structural domains. The solid lines demark the tributaries of the Oued El Rbia (South Western Meseta, SWM), of the Oued Sebou (North Western Meseta, NWM) and rivers draining directly from the

Western Meseta to the Atlantic ocean (CWM: Central Western Meseta). TMA and FMA indicate the Tabular Middle Atlas and the Folded Middle Atlas, respectively.

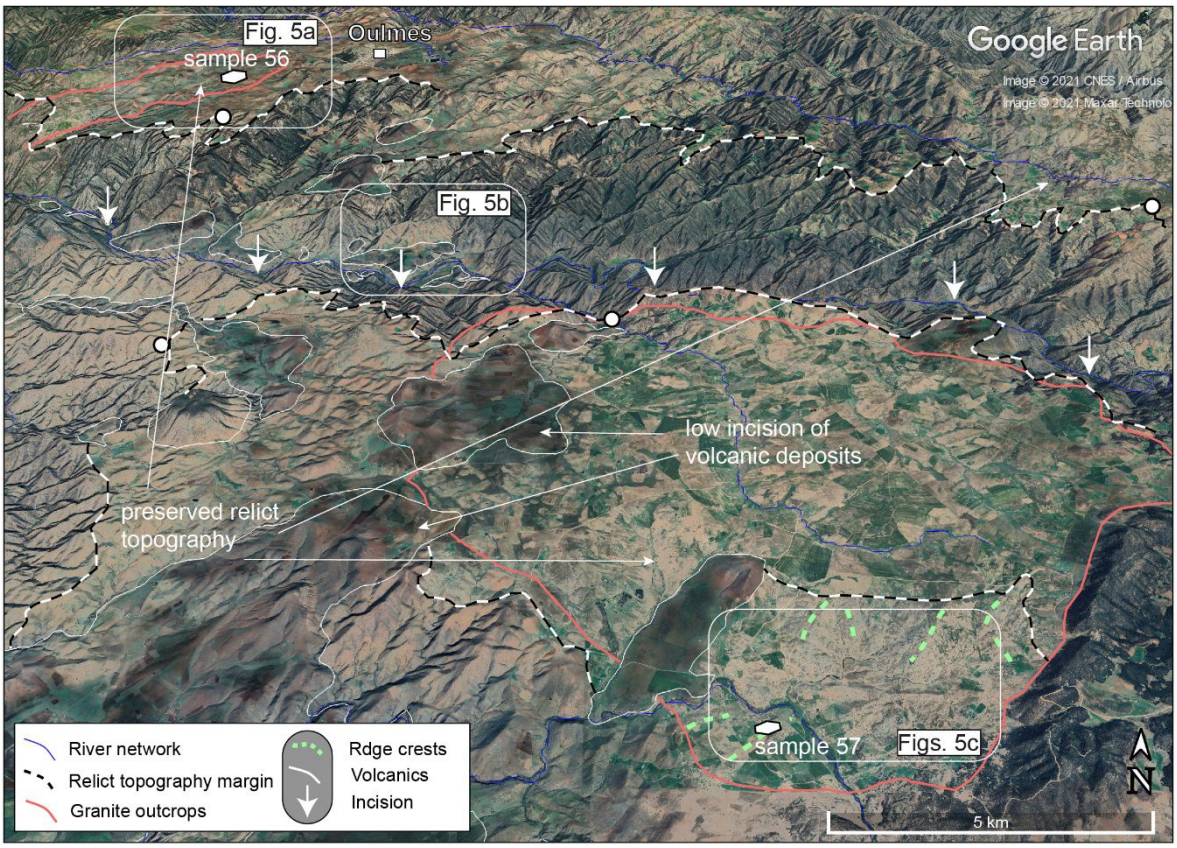

Figure 4. Prospective Google Earth view of the Western Moroccan Meseta. The granite rocks are red polygons and are located at the maximum topography over the summit erosional surface within the sampled catchments 60 and 61 (*i.e.*, relict landscape). The Pleistocene lava flows are deeply incised and well preserved in the deep incisions on the relict topography, respectively. The location of the picture is shown in figure 3.

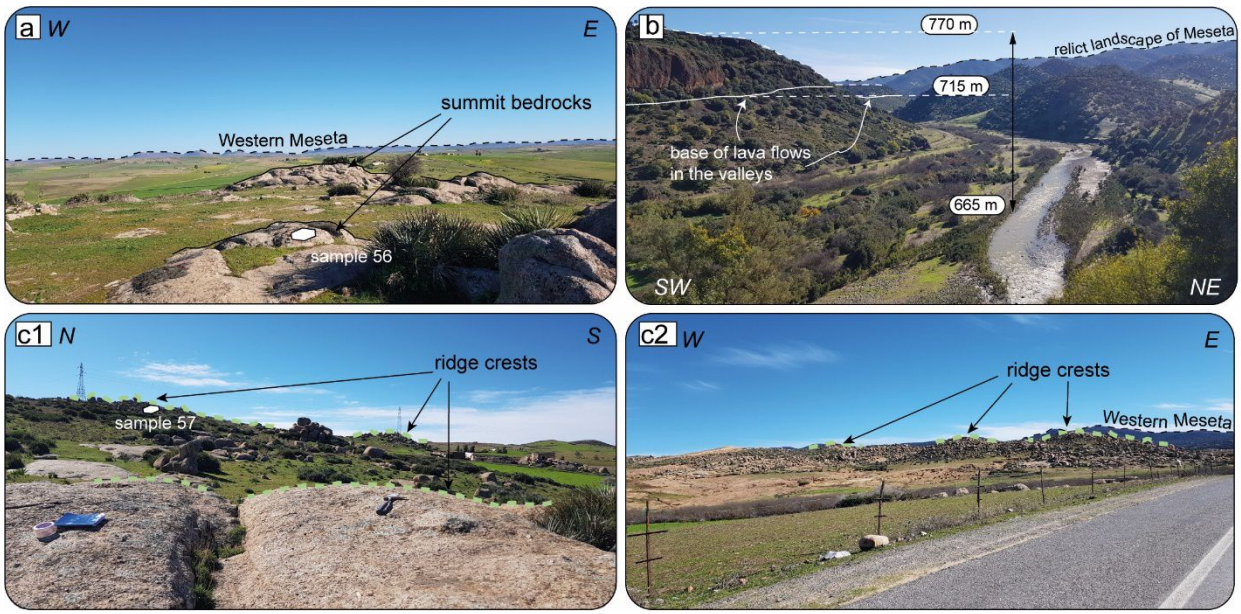

Figure 5. (a) View of the summit erosional surface of the Western Moroccan Meseta near the locality of Oulmes. The typical morphologies of the granite rocks lying at the maximum elevation are shown in the foreground (black lines). **(b)** View of the Aguennour River valley. Note the incision across the lava flow deposits (~100 and ~50 m from the top and the base of the lava flow, respectively). **(c1-c2)** View of the granite outcrops close to the plateau margin. Note the rugged morphologies related to the granite incisions (green lines). The location of the pictures is shown in figure 4.

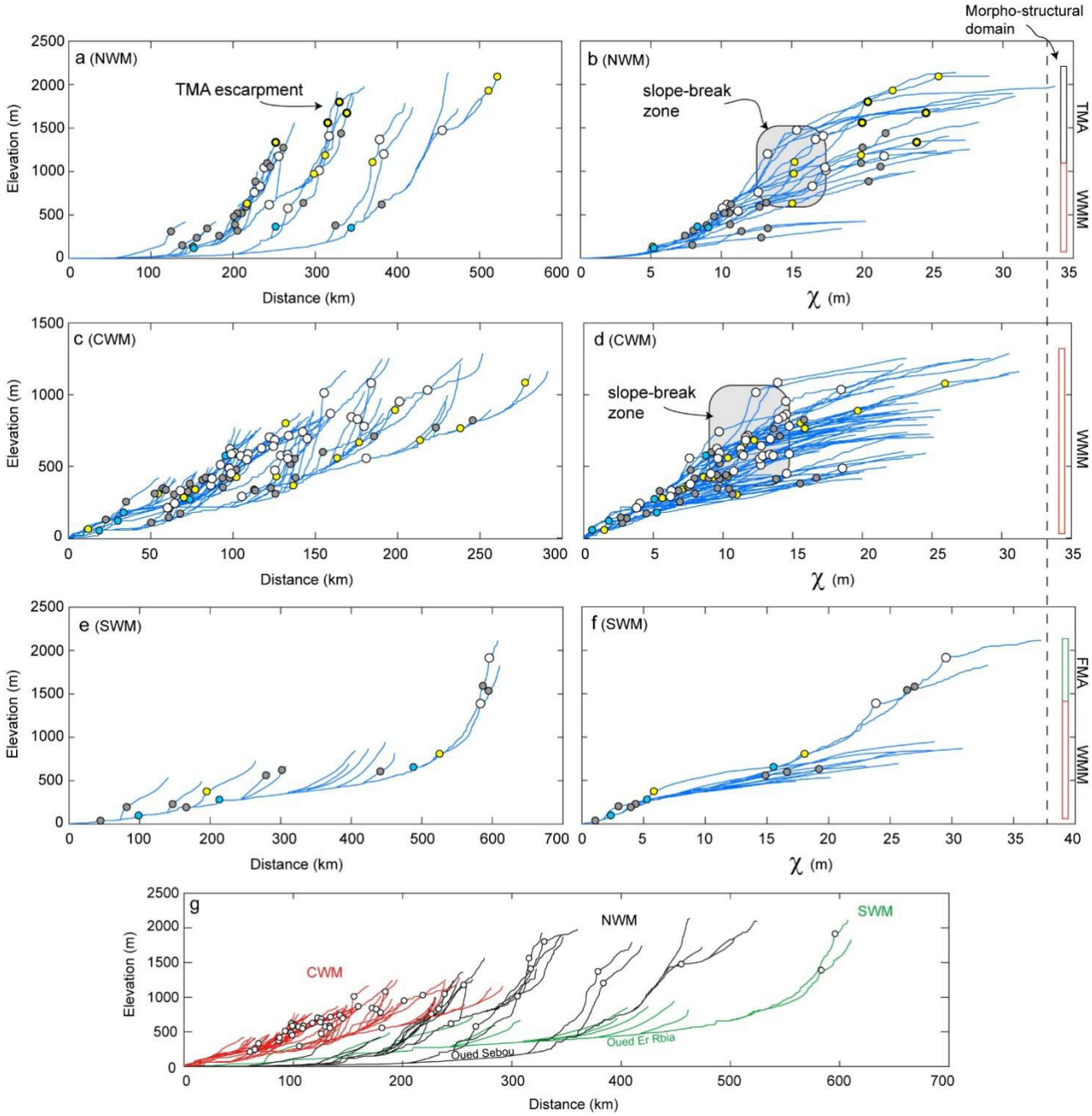

Figure 6. Longitudinal river profiles and χ-z plots with knickpoints for the NWM **(a-b)**, CWM **(c-d)**, and SWM **(e-f)**. The knickpoints legend is in figure 2a. The non-lithological knickpoints are located at the slope-break zone separating segments with different k_{sn} value. **(g)** Longitudinal river profiles with the major non-lithological knickpoints for the three morpho-structural domains. Red rivers: CWM sector; black rivers: NWM sector; green rivers: SWM sector. The non-lithological knickpoints mark the boundary between the downstream steep river profiles and the upstream low-gradient river segments, describing a paleo-surface margin. Note, the rivers of NWM and SWM sectors come mainly from the most elevated TMA and FMA domains, respectively.

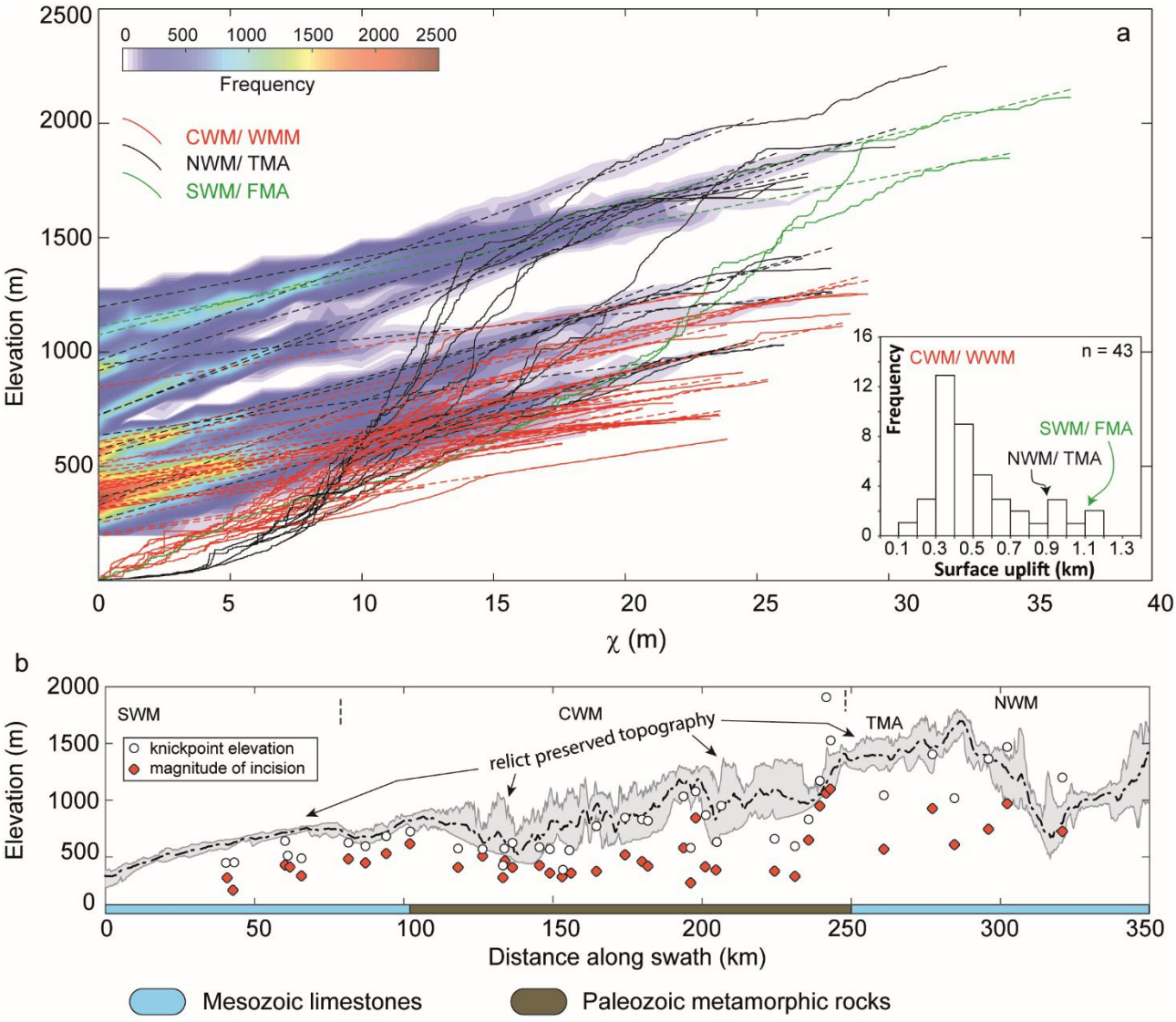

Figure 7. (a) Modern longitudinal profiles and projections of the relict landscape (black dashed segments) upstream of the highest knickpoints using $\theta_{ref} = 0.45$ and the k_{sn} of the relict portion in the χ plot. The main peaks of long-term fluvial incision are at ~400 m and ~800 m in the Western Moroccan Meseta and Tabular Middle Atlas domains, respectively (see details in Table S2). The density distribution legend is relative to the data point of the projected segments. Inset shows the frequency diagrams of the magnitude of long-term incision for the entire dataset (NWM, WMM, SWM). Note, the rivers of NWM and SWM sectors come mostly from the TMA and FMA domains, respectively. **(b)** Along-strike topographic swath profile, knickpoints elevation and magnitude of long-term incision obtained from the reconstructed river projections. SWM : South Western Meseta; CWM : Central Western Meseta; NWM : North Western Meseta; TMA : Tabular Middle Atlas. The location of the swath profile is shown in figure 3a.

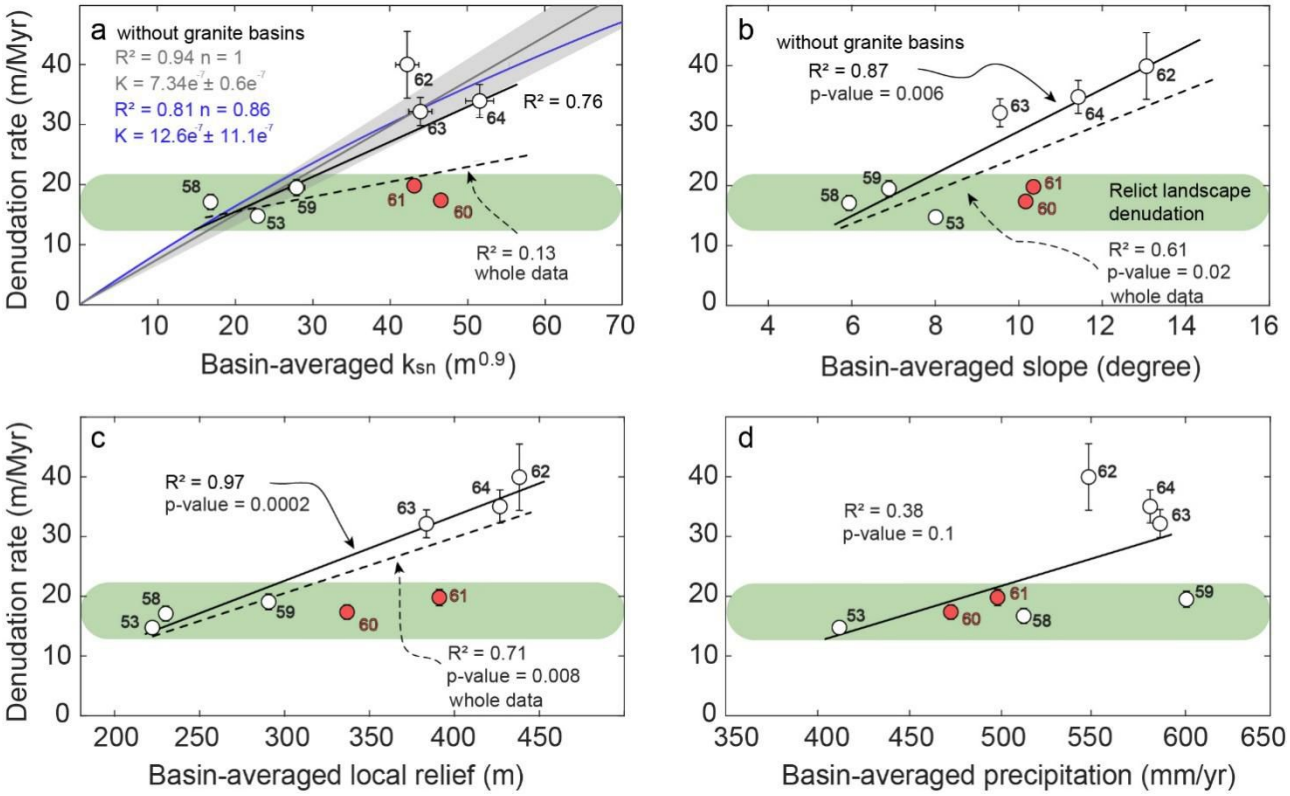

Figure 8. Basin-wide denudation rate vs basin-averaged a) k_{sn}, b) slope, c) local relief (2.5 km radius), and d) precipitation rate for the sampled basins. The black and grey solid lines show the bootstrap linear best-fit, and forced linear best-fit without considering basins with exposed granite rocks. The blue trend is the power best-fit. The dashed black lines denote the best-fit considering all sampled basins. The red circles indicate catchments characterized by the contribution of quartz from granite massifs (details in fig. 4).

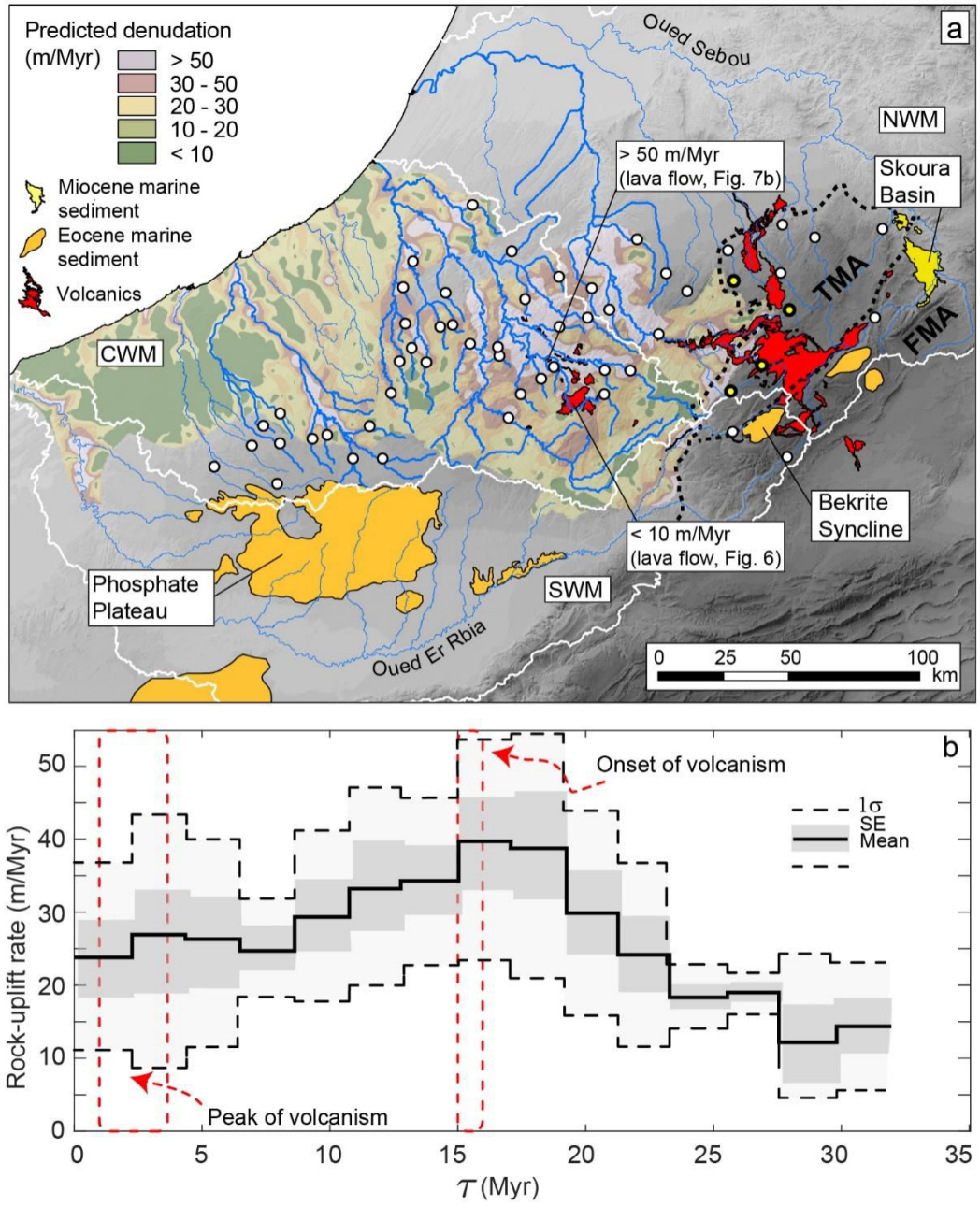

Figure 9. a) Predicted denudation rates based on the distribution of normalized channel steepness in the basement rocks. b) Rock-uplift history for selected rivers (bold blue rivers in figure 9a). Mean and standard deviation and error results from the river-profile inversion of six basins of the Western Meseta (details in Figs. S5 and S6 in supplementary material).

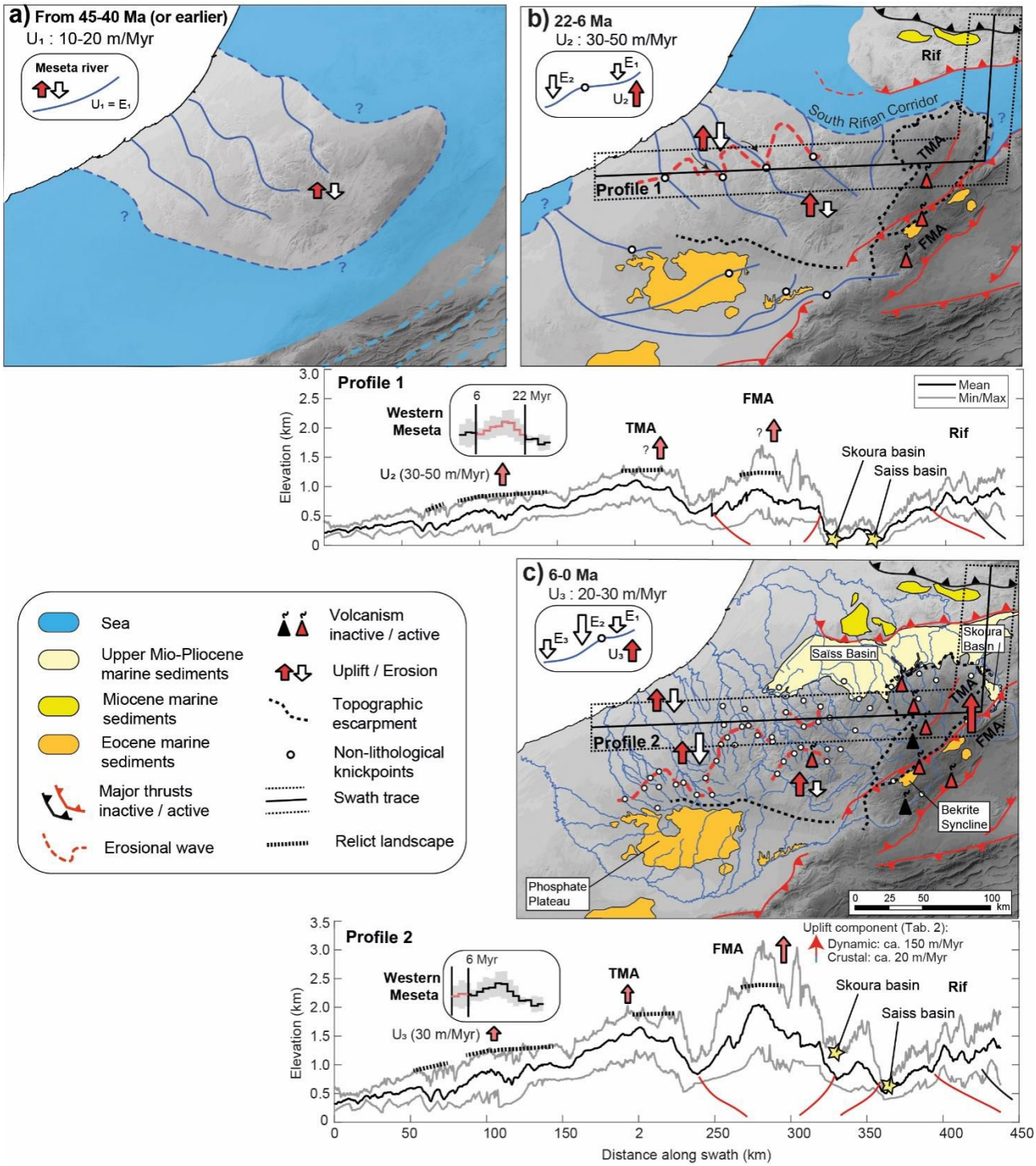

Figure 10. Schematic evolution of the Western Meseta and the Middle Atlas domains since the Lutetian (45-40 Ma). **a)** Erosional steady-state topography of the Western Meseta with marine conditions in the Middle Atlas and surrounding regions. **b)** Miocene topographic rejuvenation associated with volcanism and upstream migration of an erosional wave in response to the increase in rock-uplift rates at 22-20 Ma . Note also the southward propagation of the frontal thrusts of the Rif orogenic system with subsidence and marine deposition in the Saiss and the Skoura basins. **c)** Second slight increase in rock-uplift rates in the Western Meseta. Abrupt increase in uplift rates in the Middle Atlas as testified by uplifted marine Messinian deposits at rates of ~170 m/Myr. Inset in figures **b** and **c** show the river profiles and the inverse modelling results of the rivers flowing through the Western Meseta.

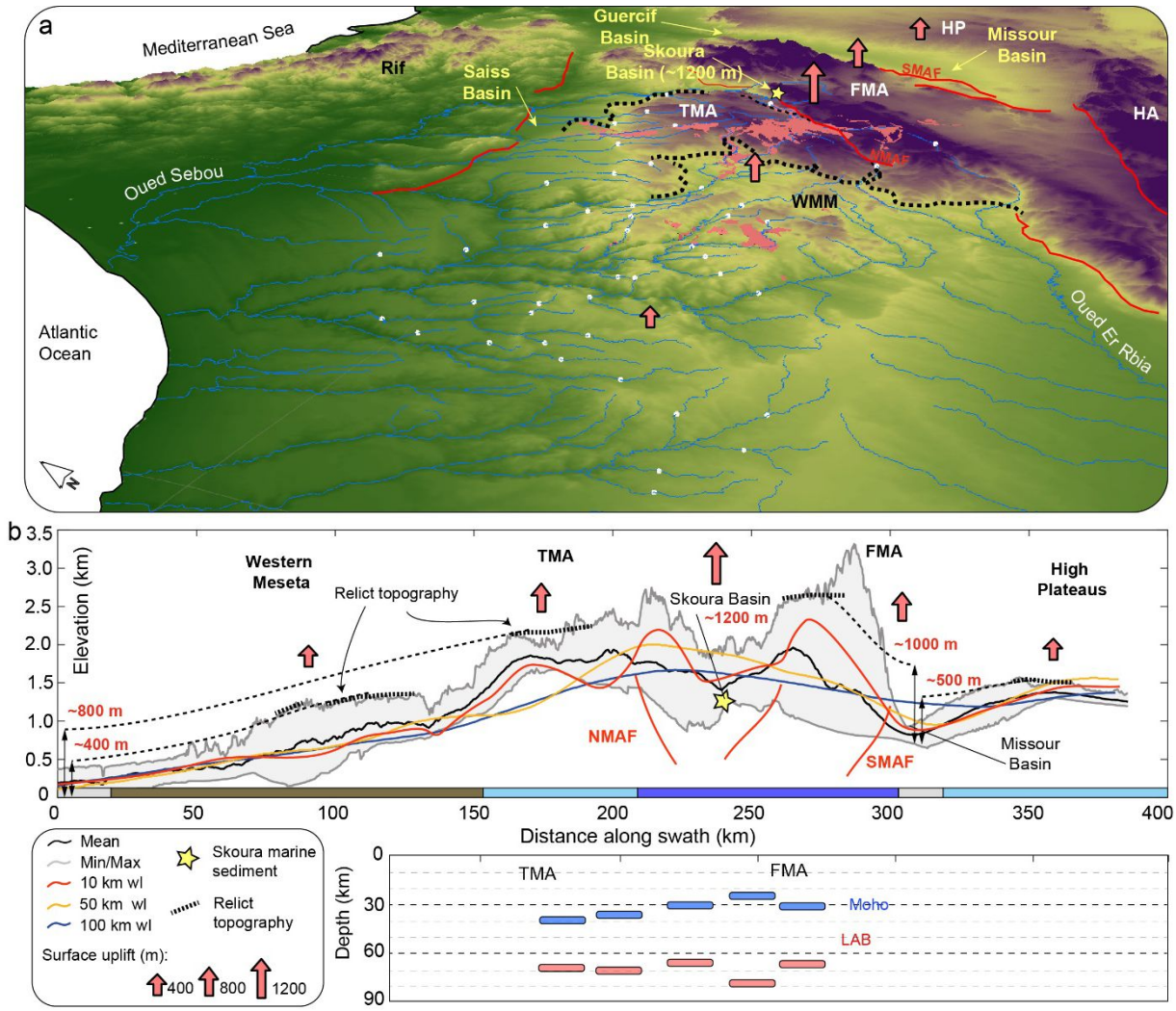

Figure 11. a) Tridimensional view of the northern Atlas-Meseta system. **b)** Swath profile (details and location are shown in Fig. 1b) with filtered topography at 10 – 50 – 100 km wavelengths and data of long-term surface uplift of WMM, TMA, FMA and HP (this work and Pastor et al., 2015). WMM: Western Moroccan Meseta; TMA and FMA: Tabular and Folded Middle Altas; HP: High Plateaus; SMAF: South Middle Atlas Fault; NMAF: North Middle Atlas Fault (after Gomez et al., 1996). The bottom panel indicates the projected position of Moho and lithosphere-asthenosphere boundary (LAB) beneath the Atlas-Meseta system from S-received functions (data from Miller and Becker, 2014).

Table 1. Denudation rates from cosmogenic ^{10}Be in river borne sand and bedrock samples.

ID	Geomorphic position	Long.	Lat.	Elev.[a]	Quarz mass[b]	Carrier mass (^{9}Be)	10Be/9Be[c]		[^{10}Be][d] 10^3 (at./g)		Production rate[e] (at./g/yr)			Denudation (m/Myr)		Integration time[f] (yr)	
		°W	°N	(m)	(g)	(g)	Value (10^{-15})	Error (%)	Value	Error	Neutrons	Slow muons	Fast muons	Value	Error	Value	Error
53	Watershed	7.1500	33.5364	455	20.70	0.151	195.1	3.4	284.7	9.8	5.08	0.015	0.04	14.76	1.02	48081	3330.1
58	Watershed	5.7512	33.2640	1173	21.82	0.150	292.6	4.3	406.0	17.6	8.69	0.02	0.05	17.11	1.27	41624	3080.5
59	Watershed	5.5714	33.3807	1083	21.68	0.151	241.6	3.4	338.5	11.7	8.16	0.02	0.05	19.49	1.35	36639	2535.6
60	Watershed	6.2790	33.4496	914	21.20	0.150	238.8	3.4	339.4	11.8	7.28	0.02	0.05	17.36	1.20	41023	2845.5
62	Watershed	5.9743	33.7520	721	21.12	0.151	95.5	12.3	135.0	17.0	6.32	0.02	0.05	39.94	5.57	18044	2514.7
Blank							0.45	51.3									
61	Watershed	6.365	33.698	928	21.47	0.152	211.5	3.3	302.7	10.3	7.35	0.02	0.05	19.80	1.37	36076	2488.0
63	Watershed	5.931	33.829	1049	21.74	0.151	146.6	4.1	204.8	8.5	7.95	0.02	0.05	32.15	2.34	22369	1630.0
56A	Summit	6.0535	33.4123	1124	21.84	0.150	1055.6	3.1	1467.4	46.0	8.43	0.02	0.05	3.46	0.23	163446	11064.1
56B	Summit	6.0535	33.4123	1124	21.59	0.150	900.1	2.5	1259.7	31.2	8.43	0.02	0.05	4.11	0.27	139446	9053.0
57A	Ridge crest	5.8906	33.1922	1098	19.45	0.150	251.2	3.3	389.0	12.9	8.23	0.02	0.05	14.36	0.98	41958	2874.7
57B	Ridge crest	5.8913	33.1919	1099	17.24	0.151	239.1	3.5	423.6	14.9	8.24	0.02	0.05	13.13	0.91	45808	3185.9
Blank							0.788	23.05									

[a] Basin mean elevation.
[b] Mass of pure quartz dissolved.
[c] Isotopic ratio uncertainties include statistical error on counted ^{10}Be events (N) and analytical error correction.
[d] Uncertainties on ^{10}Be concentrations are calculated using the standard error propagation method using the quadratic sum of the relative errors associated to the counting statistics, AMS internal error (0.5% for ASTER), and error associated to the process blank.
[e] Production rate is the spatially averaged production rate over the river basin, scaled for elevation, latitude (Stone, 2000) and geomorphic shielding (Dunne et al., 1999). The values, relative to watersheds, are calculated for a non-uniform distribution of quartz-lithologies in the sample basins (*e.g.*, Carretier et al., 2015; Clementucci et al., 2022).
[f] Integration times are calculated after Lal (1991) while their uncertainties are calculated propagating the error of the uncertainties associated with denudation rates.

Table 2. Structural topographic relief and lithospheric thickening of the Folded Middle Atlas based on the equation of Garzione et al., (2006): $dh/dt = (\rho_m - \rho_c)/\rho_c * (UH/W)$, assuming that Airy isostasy is maintained during shortening and for crustal (ρ_c) and asthenospheric mantle (ρ_m) densities of 2.8 and 3.23 kg/m^3, respectively. Shortening produces thickening and surface uplift at a rate of dh/dt (assuming no surface erosion and subsidence with deposition). The parameters H (crustal thickness) and W (orogen width) at 7 Ma and the inferred thickness after 7 Ma of shortening at rates of 0.5 to 1.5 mm/yr are consistent with modern crustal thickness data reported by Miller and Becker, (2014).

W [a] min (km)	W [a] max (km)	H [b] min (km)	H [b] max (km)	U [c] min (mm/yr)	U [c] max (mm/yr)	dh/dt [d] min (mm/yr)	dh/dt [d] max (mm/yr)
70	100	28	32	0.5	1.5	0.021	0.105
Since 7 Ma							
Elevation gain, min (km)	Elevation gain, max (km)	Crustal root [e] min (km)	Crustal root [e] max (km)	Mean thickness of crust [f] min (km)		Mean thickness of crust [f] max (km)	
0.15	0.73	0.81	3.96	28.96		36.7	

[a] Width of the deforming Middle Atlas range.
[b] Initial crustal thickness
[c] Shortening rate (data from Vernant et al., 2010 and Gomez et al., 1999).
[d] Surface uplift rate assuming lithospheric (ρ_c) and mantle (ρ_m) density of 2.8 and 3.23 kg/m^3 (after Garzione et al., 2006).
[e] Expected crustal root of the thickened crust according to Airy isostatic model (Mean gain elevation* ρ_c)/(ρ_c* ρ_m).
[f] Expected crustal thickness of the thickened crust (H + Elevation gain + Crustal root)

Supplementary materials

S1. Topographic, stream analysis

A Shuttle Radar Topography Mission Digital Elevation Model (SRTM DEM, pixel size of 30 m) was used to extract the drainage network. Hillslope metrics, such as slope and local relief with a circular sampling window of 2.5 km radius, as well as basin and channel morphometric characteristics were extracted using ArcGIS and the MATLAB software packages TopoToolbox (Schwanghart and Scherler, 2014) and Topographic Analysis Kit (TAK, Forte and Whipple, 2019), together with additional MATLAB functions (*e.g.*, Gallen, 2017).

Regions characterized by recent changes in base level retain a topographic signal in the upstream river network that provides the opportunity to evaluate the magnitude and the spatial variation of such perturbations.

The relationships between channel steepness and erosion/uplift rates have been demonstrated in various geological settings (Kirby and Whipple, 2012; Miller et al., 2013; Adams et al., 2020). In detachment-limited conditions, these relationships are modulated by the stream-power model (Howard, 1994; Whipple and Tucker, 1999). Under steady-state conditions, erosion and rock uplift rates are balanced and *dz/dt* is equal to zero, therefore the power-law can be solved as (Flint et al., 1974):

$$S = \left(\frac{E}{K}\right)^{\frac{1}{n}} A^{-\left(\frac{m}{n}\right)} \qquad (1)$$

where E is the erosion rate (*i.e.*, change in elevation (z) of a stream with respect to time (t)), A is the upstream contributing drainage area, S is the local channel slope, K is the erosional efficiency (which is function of lithology and climate), and m and n are constant values (which depend on basin hydrology, channel geometry and erosional processes). Equation (1) predicts a power relation between slope and drainage area and can be integrated, assuming E and K as spatially invariant (Perron and Royden, 2013):

$$z(x) = z(x_b) + \left(\frac{U}{KA_0^m}\right)^{\frac{1}{n}} \int_{xb}^{x} \left(\frac{A_0}{A(x)}\right)^{\frac{m}{n}} dx = z(x_b) + k_s A_0^{-\left(\frac{m}{n}\right)} \chi \qquad (2)$$

where:

$$\chi = \int_{xb}^{x} \left(\frac{A_0}{A(x')}\right)^{\frac{m}{n}} dx' \qquad (3)$$

where x_b is the base level and χ is an integral quantity, A_0 is the reference drainage area, and m/n describes the concavity of the stream. Equation (2) allows transforming river longitudinal profiles to χ versus elevation plots (here and thereafter defined as χ - z plot, where z and χ are the dependent and independent variable, respectively). Consequently, $(U/K)^{1/n}$ is the slope in the χ space, where the slope is defined as steepness index (k_s) by imposing A_0 equal to 1. The steepness index (ks) and the concavity (m/n) can be determined through the integral approach proposed by Perron and Royden, (2013). To compare ks values of longitudinal profiles, a typical reference concavity index (θ_{ref}) of 0.45, is applied to derive normalized channel steepness indices (k_{sn}; Snyder et al., 2000; Wobus et al., 2006). This value represents the best-fit concavity for all rivers draining the study area that minimizes the scatter in the χ space (Perron and Royden, 2013; Goren et al., 2014; Fig. 3h).

Knickpoints were identified and discretized along the stream network based on the shape of the streams in the longitudinal profiles, the χ - z plots and using available geological maps (Service Géologique du Maroc) and satellite imagery (Google Earth). Importantly, non-lithological, transient knickpoints cluster around similar χ values (Perron and Royden, 2013) and separate stream segments with different k_{sn} values (Kirby and Whipple, 2012; Olivetti et al., 2016; Clementucci et al., 2022). Conversely, knickpoints associated with heterogeneities along the profile and lithological contrasts are usually anchored in space and do not show a significant break in χ space (Fig. S1; Kirby and Whipple, 2012). Using this approach, the knickpoints were divided into four categories: non-lithological knickpoints, minor, lithological and dam related.

S2. ^{10}Be concentration measurements and denudation rates calculations

Samples were analyzed following a protocol including: (1) crushing (only for bedrock samples) and sieving of sand to extract the 250 – 1000 μm fraction. (2) Magnetic separation with the Frantz magnetic separator

(three steps: 0.5 - 1 – 1.5 Ampere). (3) Decarbonation of carbonate-rich samples through the reaction with HCl. (4) Leaching with HCl and H_2SiF_6 solution to remove all remaining minerals except quartz. (5) Decontamination from atmospheric ^{10}Be in the quartz grains by means of a three sequential leaching in HF. (6) Total dissolution of quartz grains, after addition of 150 µl spike of an in-house carrier of ^{9}Be carrier solution (3025 ±9 µg/g), from deep-mined phenakite crystal (Merchel et al., 2008). (7) Extraction of the final amount of Be using hydrofluoric and perchloric fuming to remove fluorides; cation and anion exchange chromatography was used to eliminate iron, aluminum, manganese, and other elements. (8) Mixing of beryllium oxide with a 325-mesh niobium powder. Measurements of in situ-produced ^{10}Be concentrations were performed at the French Accelerator mass spectrometry (AMS) national facility ASTER (Aix-en-Provence). The obtained $^{10}Be/^{9}Be$ ratios were corrected for procedural blanks and calibrated directly against the in-house STD-11 standard ($^{10}Be/^{9}Be = (1.191\pm0.013) \times 10^{-11}$; Braucher et al., 2015). Analytical uncertainties (1σ) are related to external uncertainties, variation of isotopic ratios of standards during the runs, and AMS counting statistics, and were propagated into the uncertainty of the calculated denudation rates. Finally, the basin-wide denudation rates were calculated considering the three different categories of particles responsible for the in-situ production of ^{10}Be (Braucher et al., 2011), solving analytically:

$$C(x,t) = \frac{P_n}{\lambda + \frac{\rho \cdot \varepsilon}{\Lambda_n}} \cdot e^{\frac{\rho \cdot x}{\Lambda_n}} \cdot \left(1 - e^{-\left(\lambda + \frac{\rho \cdot \varepsilon}{\Lambda_n}\right)t}\right) + \frac{P_{\mu s}}{\lambda + \frac{\rho \cdot \varepsilon}{\Lambda_{\mu s}}} \cdot e^{\frac{\rho \cdot x}{\Lambda_{\mu s}}} \cdot \left(1 - e^{-\left(\lambda + \frac{\rho \cdot \varepsilon}{\Lambda_{\mu s}}\right)t}\right) + \frac{P_{\mu f}}{\lambda + \frac{\rho \cdot \varepsilon}{\Lambda_{\mu f}}} \cdot e^{\frac{\rho \cdot x}{\Lambda_{\mu f}}} \cdot \left(1 - e^{-\left(\lambda + \frac{\rho \cdot \varepsilon}{\Lambda_{\mu f}}\right)t}\right) \quad (4)$$

where $C(x,t)$ corresponds to the nuclide concentration as a function of depth x (g/cm^2), ε (g/cm^2/yr) represents the denudation rate and t (yr) the exposure time. P_n, P_{us}, P_{uf} and Λ_m, Λ_{us}, Λ_{uf} are the production rates and effective apparent attenuation lengths of neutrons, slow muons and fast muons, respectively. Λ_n, $\Lambda_{\mu s}$, $\Lambda_{\mu f}$ values used in this paper are 160, 1500 and 4320 g/cm^2, respectively (Braucher et al., 2011), λ is the radioactive decay constant of ^{10}Be and ρ is the rock density.

Table S1. Averaged denudation rate, channel steepness, topographic slope, local relief, precipitation rate of the quartz-bearing areas exposed in the sampled basins

Sample	Basin area	Quartz-bearing area	Quartz-bearing area	Denudation rate (m/ Myr)		k_{sn} ($m^{0.9}$) [a]		Slope [b]	Local Relief[c]	Precipitation rate [d]
ID	(km^2)	(km^2)	(%)	Value	Error	Value	Error	(°)	(m)	(m/ yr)
53	535.5	228.0	42.6	14.76	1.02	22.7	0.5	8.01	222.2	411.5
58	339.3	339.3	100.0	16.66	1.23	16.7	0.6	5.9	228.4	517.9
59	970.1	496.2	51.1	19.49	1.35	27.6	0.7	6.9	288.4	599.8
60	1007.2	1007.2	100.0	17.60	1.22	46.4	0.8	10.0	337.8	472.1
61	3195.8	2775.8	86.9	19.80	1.37	43.6	1.0	10.1	381.9	495.2
62	354.5	238.9	67.4	39.94	5.57	42.4	0.9	12.9	439.9	549.6
63	3456.3	2591.5	75.0	32.15	2.34	44.4	1.0	9.8	377.4	586.3
64	-	1646.2	-	35.15	2.58	53.5	1.5	11.5	426.7	579.3

[a] Basin-averaged k_{sn} of quartz-bearing lithologies in the sampled basins.
[b] Basin-averaged slope of quartz-bearing lithologies in the sampled basins.
[c] Basin-averaged local relief (2.5 km radius) of quartz-bearing lithologies in the sampled basins.
[d] Averaged precipitation rate for the quartz-bearing lithologies areas exposed in the sampled basins.

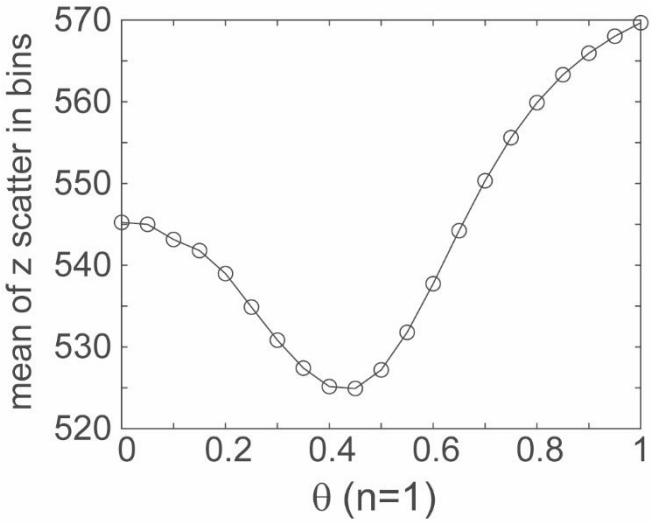

Figure S1. Plot showing the best-fit concavity index for the rivers of the study area, which is ~0.45.

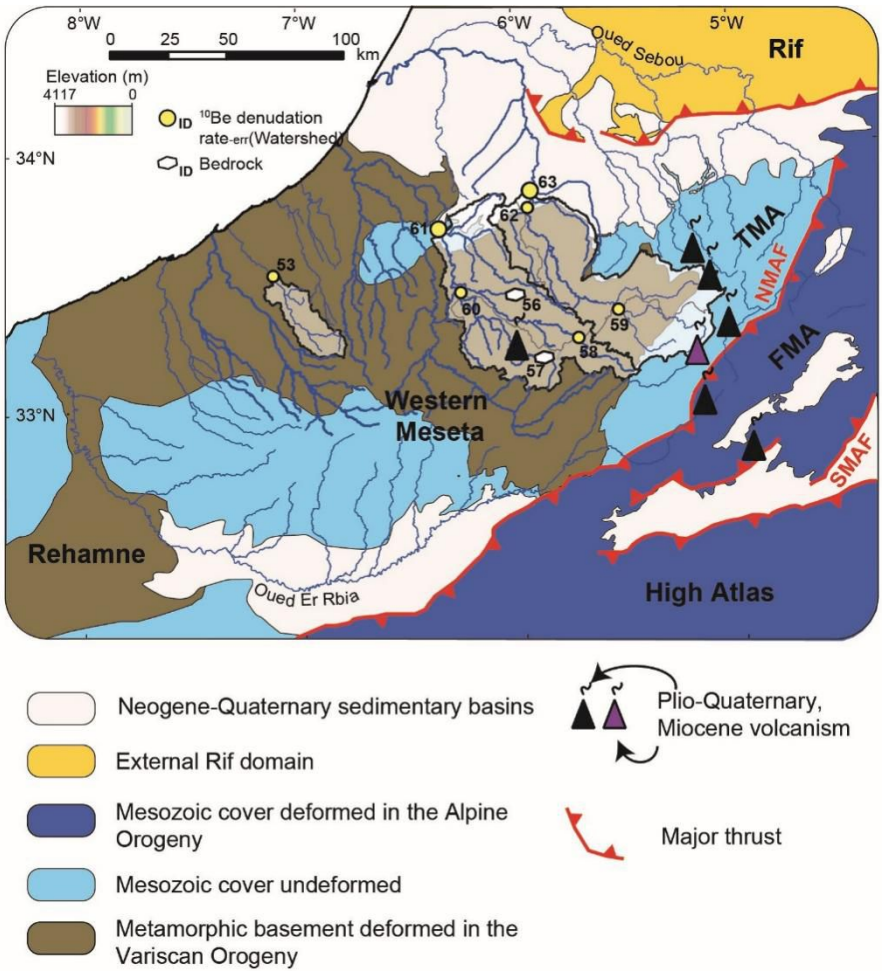

Figure S2. Morpho-structural domains in the northernwestern central Morocco and selected . FMA: Folded Middle Atlas. TMA: Tabular Middle Atlas. NMAF: North Middle Atlas fault. SMAF: South Middle Atlas fault. The white polygons are the sampling catchments. The bold blue rivers are the selected streams to perform the linear inversion.

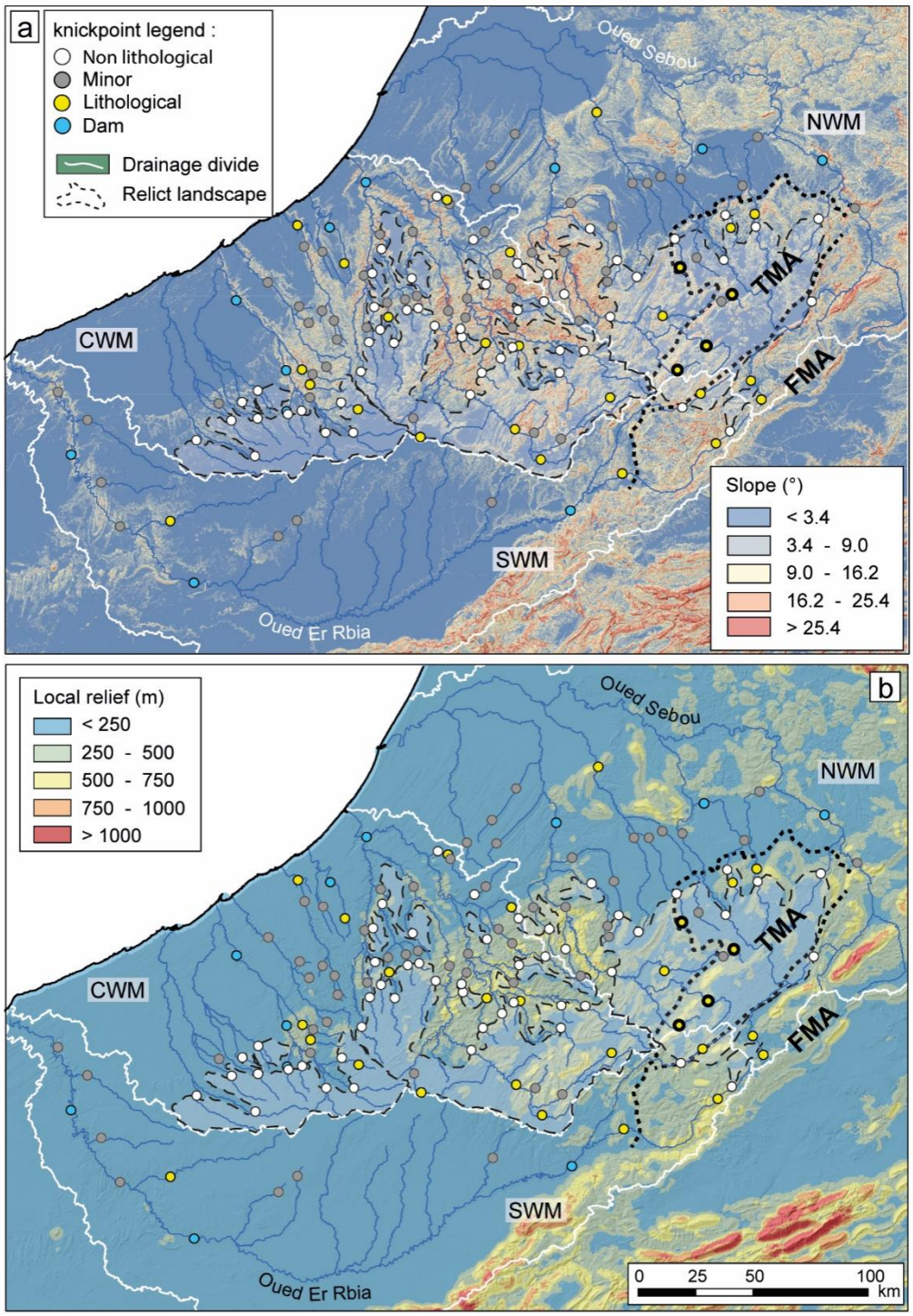

Figure S3. The slope (**a**) and local relief (2.5 km radius; **b**) maps with main knickpoints. The bold knickpoints describe the escarpment between the TMA and Moroccan Meseta, while the thick dashed line indicates the boundary between the main morpho-structural domains. The white solid lines demark the tributaries of the Oued El Rbia (South Western Meseta, SWM), of the Oued Sebou (North Western Meseta, NWM) and rivers draining directly from the Western Meseta to the Atlantic ocean (CWM: Central Western Meseta). TMA and FMA indicate the Tabular Middle Atlas and the Folded Middle Atlas, respectively.

Table S2. Non-lithological knickpoints and river profile data

Stream[a]	Long.	Lat.	Elevation	DFM[b]	DFD[c]	Drainage area	Location [d]
	°W	°N	(m)	(km)	(km)	(km^2)	
cwm1	798790.6	3686682.0	952	201.10	53.50	402.6	Meseta
cwm2	789008.6	3686828.0	1080	183.89	13.15	23.1	Meseta
cwm3	782292.6	3707195.0	870	158.74	34.06	130.0	Meseta
cwm4	771342.6	3723036.0	579	133.13	9.46	10.1	Meseta
cwm5	788862.6	3677776.0	1036	218.14	23.20	91.6	Meseta
cwm6	769298.6	3688215.0	829	175.38	13.76	22.8	Meseta
cwm7	764407.6	3683616.0	846	171.84	9.94	19.5	Meseta
cwm8	756596.6	3677849.0	780	179.56	12.64	34.1	Meseta
cwm9	788643.6	3651058.0	821	245.55	48.31	420.5	Meseta
cwm 10	737178.6	3697121.0	558	180.84	113.02	1659.8	Meseta
cwm 11	720242.6	3689894.0	624	117.30	30.97	151.4	Meseta
cwm 12	725571.6	3703691.0	587	99.21	13.76	24.6	Meseta
cwm 13	730316.6	3704348.0	570	104.67	10.10	31.1	Meseta
cwm 14	727615.6	3716685.0	372	86.58	16.31	64.2	Meseta
cwm 15	714694.6	3695588.0	575	109.39	16.58	32.6	Meseta
cwm 16	709949.6	3690259.0	550	108.05	19.47	68.3	Meseta
cwm 17	711993.6	3704932.0	417	87.22	10.62	16.5	Meseta
cwm 18	711190.6	3718875.0	380	68.00	10.91	16.9	Meseta
cwm 19	706737.6	3678141.0	573	128.93	28.52	197.5	Meseta
cwm 20	699656.6	3723255.0	309	64.17	14.03	28.9	Meseta
cwm 21	703379.6	3652810.0	715	133.85	27.29	177.1	Meseta
cwm 22	691918.6	3652883.0	683	125.31	18.69	110.4	Meseta
cwm 23	682063.6	3662008.0	594	100.79	15.43	48.6	Meseta
cwm 24	676369.6	3660548.0	625	98.17	20.55	84.8	Meseta
cwm 25	664032.6	3670330.0	450	98.74	37.46	187.6	Meseta
cwm 26	657389.6	3665585.0	486	97.54	8.08	9.7	Meseta
cwm 27	652936.6	3657920.0	510	92.40	23.13	69.1	Meseta
cwm 28	662791.6	3643247.0	641	124.46	30.87	215.0	Meseta
cwm 29	638628.6	3649817.0	450	97.60	14.43	42.9	Meseta
cwm 30	663813.6	3658869.0	586	109.10	17.52	84.7	Meseta
cwm 31	698415.6	3665439.0	702	122.12	20.19	65.5	Meseta
cwm 32	715059.6	3728876.0	208	60.65	87.61	766.1	Meseta
cwm 33	748347.6	3692522.0	742	142.19	9.29	18.5	Meseta
cwm 34	737178.6	3697121.0	558	133.22	28.75	124.6	Meseta
cwm 35	747836.6	3695880.0	695	145.04	9.45	16.7	Meseta
cwm 36	771561.6	3703691.0	1012	155.34	15.27	33.6	Meseta
cwm 37	753092.6	3732745.0	290	105.40	33.15	175.7	Meseta
cwm 38	742945.6	3747564.0	331	72.90	14.93	42.9	Meseta
Mean wmm			621 ± 121				
nwm1	800323.6	3705808.0	618	243.97	118.61	2097.4	Meseta
nwm2	892887.6	3707268.0	1475	454.62	84.77	1351.2	TMA
nwm3	895734.6	3741505.0	1202	383.38	48.15	290.2	TMA
nwm4	869965.6	3738074.0	1369	378.39	33.77	198.9	TMA
nwm5	857336.6	3743038.0	1013	304.82	20.06	76.4	TMA
nwm6	856752.6	3724350.0	1408	316.88	31.22	148.9	TMA
nwm7	820544.6	3717415.0	1175	255.61	10.79	35.3	TMA
nwm8	836385.6	3733110.0	1045	237.99	19.01	59.4	TMA
nwm9	783898.6	3718510.0	632	217.02	15.62	45.1	Meseta
nwm10	928949.6	3707560.0	1348	441.63	49.22	410.3	TMA
nwm11	812514.6	3724131.0	830	232.77	19.43	105.9	Meseta
nwm12	801272.6	3737344.0	545	201.53	31.10	103.6	Meseta
nwm13	790687.6	3710261.0	761	225.87	21.69	64.6	Meseta
Mean nwm			1032 ± 188				

swm1	859161.6	3653467.0	1915	595.72	13.29	57.7	FMA
swm2	847262.6	3670914.0	1532	595.71	19.90	84.9	FMA
Mean swm	798790.6	3686682.0	1724 ± 135				
Mean Meseta			627 ± 116				
Mean TMA			1255 ± 86				
Mean FMA			1724 ± 135				

[a] cwm : river draining directly to the ocean; nwm : river draining into the Oued Sebou; swm : river draining into the Oued Er Rbia.
[b] Distance from divide.
[c] Distance from river mouth
[d] Meseta : rivers draining the Western Moroccan Meseta sectors (WMM); TMA: rivers draining the Tabular Middle Atlas (NWM sector). FMA: rivers draining the Folded Middle Atlas (SWM sector).

Table S3. Reconstructed relict stream profile and 95% confidence interval

Stream[a]	m/n	Elevation knickpoint	ΔZ[b]	Error (2σ)	Location[b]
		(m)	(m)	(m)	
cwm1	0.45	952	608.2	10.1	Meseta
cwm2	0.45	1080	845.3	2.7	Meseta
cwm3	0.45	870	404.8	6.3	Meseta
cwm4	0.45	579	252.3	11.8	Meseta
cwm5	0.45	1036	570.8	14.2	Meseta
cwm6	0.45	829	447.0	15.7	Meseta
cwm7	0.45	846	506.5	6.9	Meseta
cwm8	0.45	780	356.8	9.5	Meseta
cwm9	0.45	821	396.7	3.8	Meseta
cwm 10	0.45	558	332.5	6.5	Meseta
cwm 11	0.45	624	396.6	4.1	Meseta
cwm 12	0.45	587	423.5	4.7	Meseta
cwm 13	0.45	570	341.5	13.1	Meseta
cwm 14	0.45	372	310.7	14.1	Meseta
cwm 15	0.45	575	457.8	4.1	Meseta
cwm 16	0.45	550	497.4	7.0	Meseta
cwm 17	0.45	417	309.5	13.9	Meseta
cwm 18	0.45	380	341.4	4.1	Meseta
cwm 19	0.45	573	399.0	22.0	Meseta
cwm 20	0.45	309	193.7	14.8	Meseta
cwm 21	0.45	715	602.0	1.1	Meseta
cwm 22	0.45	683	521.9	1.3	Meseta
cwm 23	0.45	594	430.3	6.8	Meseta
cwm 24	0.45	625	475.9	2.5	Meseta
cwm 25	0.45	450	203.9	1.4	Meseta
cwm 26	0.45	486	319.2	9.0	Meseta
cwm 27	0.45	510	413.5	8.7	Meseta
cwm 28	0.45	641	428.1	4.6	Meseta
cwm 29	0.45	450	313.6	4.9	Meseta
Mean wmm			417.3	54.9	
nwm1	0.45	618	328.4	17.8	Meseta
nwm2	0.45	1475	961.3	26.9	TMA
nwm3	0.45	1202	722.4	22.6	TMA
nwm4	0.45	1369	725.1	23.8	TMA
nwm5	0.45	1013	574.3	41.3	TMA
nwm6	0.45	1408	917.7	23.3	TMA
nwm7	0.45	1175	944.3	12.6	TMA
nwm8	0.45	1045	544.8	28.1	TMA
nwm9	0.45	632	363.1	24.6	Meseta
nwm10	0.45	1348	1196.1	17.6	TMA
nwm11	0.45	830	635.6	24.1	Meseta
nwm12	0.45	545	265.1	27.1	Meseta
Mean nwm			681.5	86.4	
swm1	0.45	1915	1067.0	37.8	FMA
swm2	0.45	1532	1105.4	89.6	FMA
Mean swm			1086.2	63.7	
Mean Meseta			414.9	54.9	
Mean TMA			823.2	66.5	
Mean FMA			1086.2	63.7	

[a] cwm : river draining directly to the ocean; nwm : river draining into the Oued Sebou; swm : river draining into the Oued Er Rbia.
[b] Estimated long-term fluvial incision from reconstructed relict stream profiles.
[c] Meseta domains : rivers draining the Western Moroccan Meseta domain (mostly from cwm and nwm sector); TMA: rivers draining the Tabular Middle Atlas (mostly nwm sectors); FMA: rivers draining the Folded Middle Atlas (from swm sector).

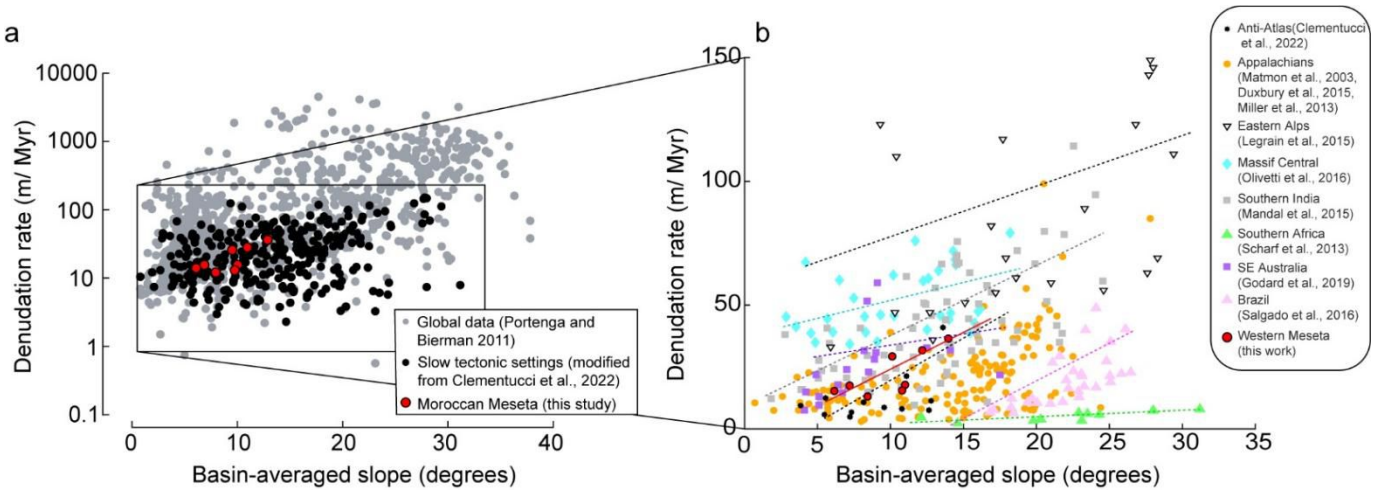

Figure S4. Global compilation of basin-averaged slope versus basin-wide denudation rates for slow tectonic settings (modified from Olivetti et al., 2016; Clementucci et al., 2022).

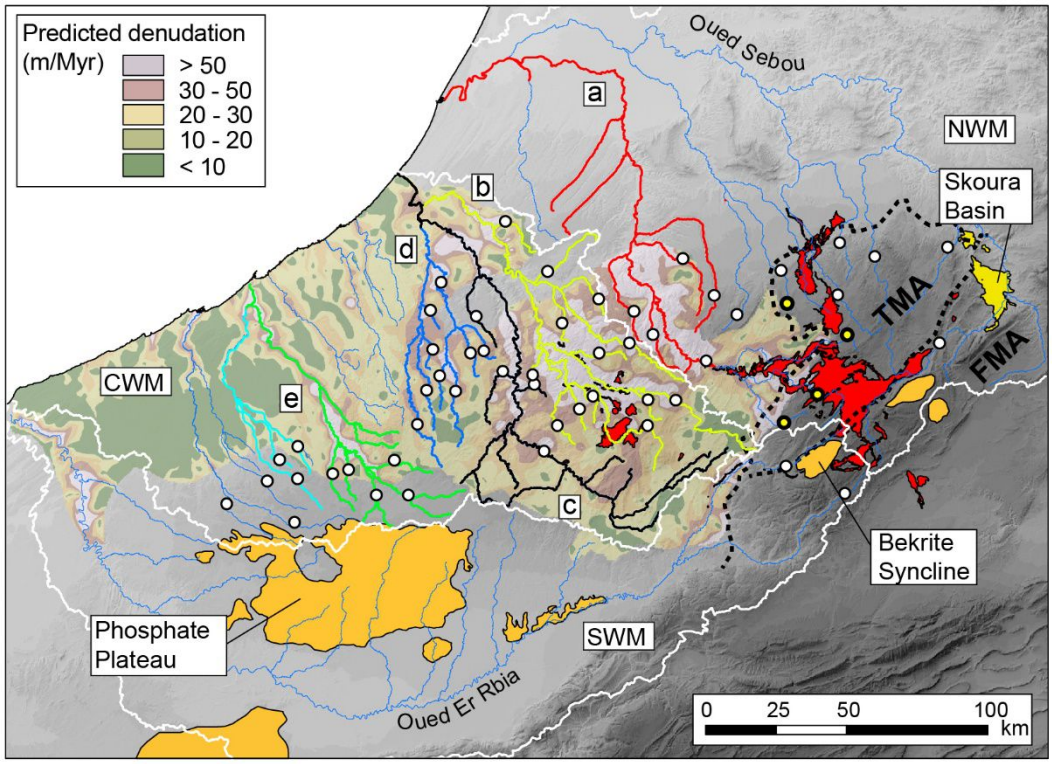

Figure S5. Predicted denudation rates based on the distribution of normalized channel steepness in the basement rocks. The colored rivers represent the catchments selected for the linear inversion (details in fig. S6).

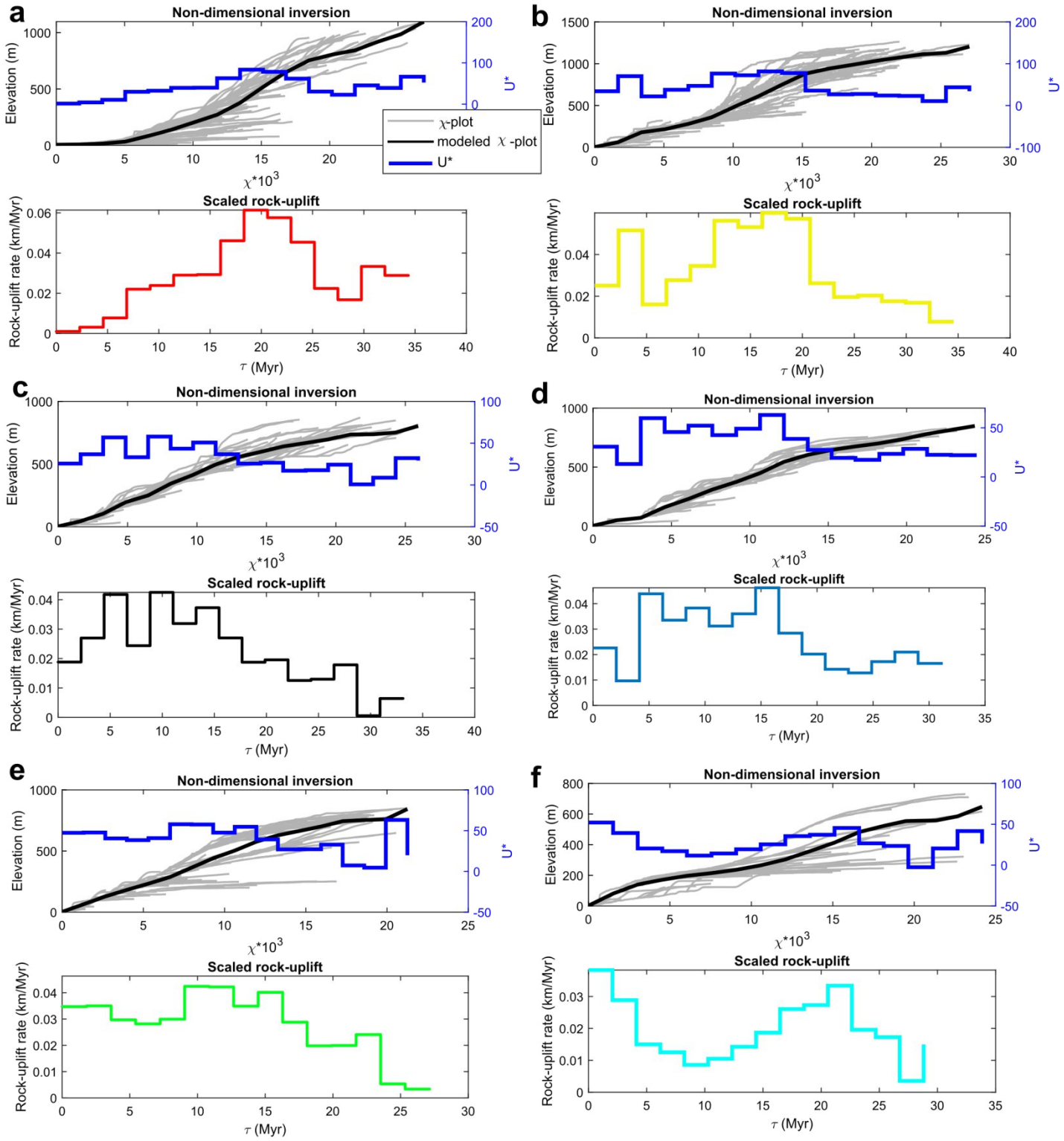

Figure S6. River-profile inversion of six basins of the Western Meseta. The river inversions are constrained using the mean erodibility value of basement rocks, n = 1 and m/n = 0.45. In the bottom τ-plots, the thick transparent trends represent the river inversion results from $K \pm 1\sigma$ ($7.34 \pm 0.58 * 10^{-7}$ $m^{0.1}$/yr). Location of selected rivers is shown in figure S5 through the colour scale.

References

Adams, B. A., Whipple, K. X., Forte, A. M., Heimsath, A. M., Hodges, K. V., 2020. Climate controls on erosion in tectonically active landscapes. Sci. adv. 6(42), eaaz3166. https://www.science.org/doi/10.1126/sciadv.aaz3166.

Braucher, R., Merchel, S., Borgomano, J., Bourlès, D. L., 2011. Production of cosmogenic radionuclides at great depth: A multi element approach. Earth Planet. Sci. Lett. 309(1-2), 1-9. https://doi.org/10.1016/j.epsl.2011.06.036.

Braucher, R., Guillou, V., Bourlès, D. L., Arnold, M., Aumaître, G., Keddadouche, K., Nottoli, E., 2015. Preparation of ASTER in-house 10Be/9Be standard solutions. Nucl. Instrum. Methods Phys. Res., Sect. Beam Interactions with Materials and Atoms. 361, 335-340. https://doi.org/10.1016/j.nimb.2015.06.012.

Carretier, S., Regard, V., Vassallo, R., Martinod, J., Christophoul, F., Gayer, E., Audin L., Lagane, C., 2015. A note on 10Be-derived mean erosion rates in catchments with heterogeneous lithology: Examples from the western Central Andes. Earth Surf. Process. Landf. 40(13), 1719-1729. https://doi.org/10.1002/esp.3748.

Clementucci R., Ballato P., Siame L., Faccenna C., Yaaqoub A., Essaifi A., Leanni L., Guillou V., 2022. Lithological control on topographic relief evolution in a slow tectonic setting (Anti-Atlas, Morocco). Earth and Planet. Sci. Lett. https://doi.org/10.1016/j.epsl.2022.117788.

Dunne, J., Elmore, D., Muzikar, P., 1999. Scaling factors for the rates of production of cosmogenic nuclides for geometric shielding and attenuation at depth on sloped surfaces. Geomorphology. 27(1-2), 3-11. https://doi.org/10.1016/S0169-555X(98)00086-5.

Duxbury, J., Bierman, P. R., Portenga, E. W., Pavich, M. J., Southworth, S., Freeman, S. P., 2015. Erosion rates in and around Shenandoah National Park, Virginia, determined using analysis of cosmogenic 10Be. American Journal of Science, 315(1), 46-76. https://doi.org/10.2475/01.2015.02.

Flint, J. J., 1974. Stream gradient as a function of order, magnitude, and discharge. Water Resources Research, 10(5), 969-973. https://doi.org/10.1029/WR010i005p00969.

Forte, A.M., Whipple, K.X., 2019. Short communication: the Topographic Analysis Kit (TAK) for TopoToolbox. Earth Surf. Dyn.7, 87–95. https://doi.org/10.5194/esurf-7-87-2019.

Gallen, S. F., 2018. Lithologic controls on landscape dynamics and aquatic species evolution in post-orogenic mountains. Earth and Planet. Sci. Lett. 493, 150-160. https://doi.org/10.1016/j.epsl.2018.04.029.

Godard, V., Dosseto, A., Fleury, J., Bellier, O., Siame, L., ASTER Team., 2019. Transient landscape dynamics across the Southeastern Australian Escarpment. Earth and Planet. Sci. Lett. 506, 397-406. https://doi.org/10.1016/j.epsl.2018.11.017.

Goren, L., Fox, M., Willett, S. D., 2014. Tectonics from fluvial topography using formal linear inversion: Theory and applications to the Inyo Mountains, California. . J. Geophys. Res., Earth Surface, 119(8), 1651-1681. https://doi.org/10.1002/2014JF003079.

Granger, D. E., Kirchner, J. W., Finkel, R., 1996. Spatially averaged long-term erosion rates measured from in situ-produced cosmogenic nuclides in alluvial sediment. The J. Geol. 104(3), 249-257. http://www.jstor.org/stable/30068190.

Howard, A.D., Kerby, G., 1983. Channel changes in badlands. Geol. Soc. Am. Bull.94, 739–752. http://dx.doi.org/10.1130/0016-7606(1983)94<739:CCIB>2.0.CO;2.

Kirby, E., Whipple, K. X., 2012. Expression of active tectonics in erosional landscapes. J. Struct. Geol. 44, 54-75. https://doi.org/10.1016/j.jsg.2012.07.009.

Legrain, N., Dixon, J., Stüwe, K., von Blanckenburg, F., Kubik, P., 2015. Post-Miocene landscape rejuvenation at the eastern end of the Alps. Lithosphere, 7(1), 3-13. https://doi.org/10.1130/L391.1.

Mandal, S. K., Lupker, M., Burg, J. P., Valla, P. G., Haghipour, N., Christl, M., 2015. Spatial variability of 10Be-derived erosion rates across the southern Peninsular Indian escarpment: A key to landscape evolution across passive margins. Earth and Planet. Sci. Lett., 425, 154-167. https://doi.org/10.1016/j.epsl.2015.05.050.

Matmon, A., Bierman, P. R., Larsen, J., Southworth, S., Pavich, M., Caffee, M., 2003. Temporally and spatially uniform rates of erosion in the southern Appalachian Great Smoky Mountains. Geology, 31(2), 155-158. https://doi.org/10.1130/0091-7613(2003)031<0155:TASURO>2.0.CO;2.

Merchel, S., Arnold, M., Aumaître, G., Benedetti, L., Bourlès, D. L., Braucher, R., Alfimov V., Freeman S.P.H.T., Steier P., Wallner, A., 2008. Towards more precise ^{10}Be and ^{36}Cl data from measurements at the 10− 14 level: Influence of sample preparation. Nucl. Instrum. Methods Phys. Res., Sect. Beam Interactions with Materials and Atoms. 266(22), 4921-4926. https://doi.org/10.1016/j.nimb.2008.07.031.

Miller, S. R., Sak, P. B., Kirby, E., Bierman, P. R., 2013. Neogene rejuvenation of central Appalachian topography: Evidence for differential rock uplift from stream profiles and erosion rates. Earth and Planet. Sci. Lett., 369, 1-12.

Olivetti, V., Godard, V., Bellier, O., ASTER team., 2016. Cenozoic rejuvenation events of Massif Central topography (France): Insights from cosmogenic denudation rates and river profiles. Earth and Planet. Sci. Lett., 444, 179-191. https://doi.org/10.1016/j.epsl.2016.03.049.

Perron, J.T., Royden, L., 2013. An integral approach to bedrock river profile analysis. Earth Surf. Process. Landf. 38, 570–576. https://doi.org/10.1002/esp.3302.

Salgado, A. A. R., de Andrade Rezende, E., Bourles, D., Braucher, R., da Silva, J. R., Garcia, R. A., 2016. Relief evolution of the Continental Rift of Southeast Brazil revealed by in situ-produced 10Be concentrations in river-borne sediments. Journal of South American Earth Sciences, 67, 89-99. https://doi.org/10.1016/j.jsames.2016.02.002

Scharf, T. E., Codilean, A. T., De Wit, M., Jansen, J. D., Kubik, P. W., 2013. Strong rocks sustain ancient postorogenic topography in southern Africa. Geology, 41(3), 331-334. https://doi.org/10.1130/G33806.1.

Schwanghart, W., Scherler, D., 2014. Short communication: TopoToolbox 2 – MATLAB-based software for topographic analysis and modeling in Earth surface sciences. Earth Surf. Dyn.2, 1–7. https://doi.org/10.5194/esurf-2-1-2014.

Stone, J. O., 2000. Air pressure and cosmogenic isotope production. J. Geophys. Res., Solid Earth. 105(B10), 23753-23759. https://doi.org/10.1029/2000JB900181.

Whipple, K.X., Tucker, G.E., 1999. Dynamics of the stream-power river incision model: implications for height limits of mountain ranges, landscape response timescales, and research needs. J. Geophys. Res., Solid Earth. 104, 17661–17674. https://doi.org/10.1029/1999JB900120.